Comparative analysis of CO_2 and propane heat pumps for water heating seasonal performance of air and hybrid solar-air systems

Conte, Riccardo; Zanetti, Emanuele; Tancon, Marco; Azzolin, Marco

DOI
10.1016/j.applthermaleng.2025.127131

Publication date
2025

Document Version
Final published version

Published in
Applied Thermal Engineering

Applied Thermal Engineering 278 (2025) 127131

Contents lists available at ScienceDirect

Applied Thermal Engineering

journal homepage: www.elsevier.com/locate/apthermeng

Research Paper

Comparative analysis of CO_2 and propane heat pumps for water heating: seasonal performance of air and hybrid solar-air systems☆

Riccardo Conte [a], Emanuele Zanetti [b], Marco Tancon [a], Marco Azzolin [a,*]

[a] Department of Industrial Engineering, University of Padova, Via Venezia 1, 35131 Padova, Italy
[b] Department of Process and Energy, Delft University of Technology, Leeghwaterstraat 39, 2628 CB Delft, the Netherlands

ARTICLE INFO

Keywords:
Natural refrigerants
Dual-source solar-air heat pump
Space heating
Domestic hot water
Seasonal performance
PV-T

ABSTRACT

This study numerically compares the seasonal heating performance (SCOP) of three 15 kW heat pumps using natural refrigerants: two with carbon dioxide and one with propane. The propane system is an air-source heat pump (R290-AHP). The carbon dioxide systems include an air-source heat pump (R744-AHP) and a dual-source solar-air heat pump (R744-SAHP) equipped with finned-coil and photovoltaic-thermal evaporators that can work simultaneously. In the case of a transcritical carbon dioxide cycle, the use of several low-temperature sources is a promising solution to improve the performance of the system by enhancing the exploitation of renewable energy sources. Since the efficiency of air and solar-based systems is related to weather conditions and location, there is the need for accurate models to evaluate the SCOP. In this work, a numerical model has been developed to design the three 15 kW heat pumps and assess the SCOPs under variable space heating and domestic hot water demand profiles, using climatic data for Rome and Strasbourg. The results indicate that the R290-AHP consistently achieves the highest SCOP, while the R744-AHP performs the lowest. The R744-SAHP overperforms the R744-AHP by approximately 4 % regardless of heating demand characteristics. In particular, the results show that the performance of the three heat pumps is significantly influenced by the distribution of the thermal load throughout the day. Specifically, when the thermal load is concentrated during daylight hours, the heat pumps can operate at a higher SCOP, especially for the R744-SAHP, and also increase, up to 44 %, the self-consumed photovoltaic energy produced.

1. Introduction

Space and water heating accounted for almost half of building energy use in 2022, with 63 % powered by fossil fuels, producing around 2.400 Mt of direct CO_2 emissions [1]. Heat pumps, powered by low-emissions electricity, are considered the central technology in the global transition to secure and sustainable heating [2]. The sustainability of these systems is not limited to the replacement of fossil fuel consumption with electric consumption; it is also contingent on the adoption of environmentally friendly refrigerants with low global warming potential (GWP). In this scenario, the replacement of high GWP hydrofluorocarbon (HFC) refrigerants with ultra-low GWP natural refrigerants is of critical importance.

These efforts are also being driven by recent actions, such as the new European Union's F-gas Regulation (EU) 2024/573 [3]. In the near future, for an increasing number of applications, heat pumps will have to work with natural refrigerants, such as CO_2 (R744) and propane (R290). These refrigerants are characterized by low GWP, zero ozone-depleting potential and non-toxicity. In the case of propane, its properties allow it to reach superior heat transfer coefficients as compared to conventional refrigerants such as R134 and R22, but also equivalent [4] or higher coefficient of performance (COP), up to 5 % [5,6]. Compared to other refrigerants, R744 offers advantages such as reduced compressor and piping dimensions due to its high density and volumetric cooling capacity. Nevertheless, they have some drawbacks: R290 is highly flammable, whereas R744 heat pumps have to withstand higher pressure and perform a transcritical cycle when facing space heating (SH) and domestic hot water (DHW) demands. R290 and R744 do not necessarily compete as they are suited for different applications.

The R744 refrigerant is usually employed in heat pumps operating with a transcritical cycle, making it an efficient solution for the heating of water with high-temperature lifts. However, in order to optimize the COP, it is crucial to keep the inlet water temperature at the gas-cooler as

☆ This article is part of a special issue entitled: 'SDEWES 2024' published in Applied Thermal Engineering.

* Corresponding author at: University of Padova, Department of Industrial Engineering Via Venezia 1, 35131 Padova, Italy.
E-mail address: marco.azzolin@unipd.it (M. Azzolin).

https://doi.org/10.1016/j.applthermaleng.2025.127131
Received 26 January 2025; Received in revised form 17 May 2025; Accepted 4 June 2025
Available online 6 June 2025

Nomenclature

Symbols

A	Area [m^2]
b	Slope of saturated air enthalpy [J/(kg K)]
c	Specific heat [J/(kg K)]
D	Diameter [m]
E	Energy [Wh]
G	Solar irradiance on the tilted plane of the PV-T collector [W/m^2]
h	Specific enthalpy [J/kg]
H	Height [m]
HTC	Local heat transfer coefficient [$W/(m^2 K)$]
K	Global heat transfer coefficient [$W/(m^2 K)$]
l	Thickness [m]
L	Tube length [m]
$\dot{m}$	Mass flow rate [kg/s]
N_d	Number of longitudinal elements in which each tube is discretized [-]
N_t	Number of tube per row [-]
p	Pressure [bar]
P	Electrical power [W]
Q	Heat flow rate [W]
T	Temperature [°C]
V	Volume [m^3]
x	Vapor quality [-]

Greek symbols

Δ	Difference [-]
δ	Thickness of the condensed liquid film [m]
ε	Finned coil efficiency [-]
η	Efficiency [-]
λ	Thermal conductivity [W/(m K)]
ρ	Density [kg/m^3]

Subscripts

air	Air
cell	Photovoltaic cell
cond	Conduction
COND	Condensation
conv	Convection
evap	Evaporation
ext	External
f	Fin
fs	Fin surface
i	Tank layer
in	Inlet
int	Internal
j	Element
out	Outlet
r	Refrigerant
self	Self-consumption
th	Thermal
tot	Total
w	Water

Acronyms

AHP	Air Heat Pump
COMP	Compressor
COND	Condenser
COP	Coefficient Of Performance
DHW	Domestic hot water
EEV	Electronic expansion valve
FC-HE	Finned coil heat exchanger
GC	Gas-cooler
GWP	Global Warming Potential
HFC	Hydrofluorocarbon
HP	Heat pump
IHE	Internal heat exchanger
NOCT	Nominal Operating Cell Temperature
PV	Photovoltaic module
PV-T	Photovoltaic-thermal collector
REC	Low pressure receiver
SAHP	Solar-Air Heat Pump
SCOP	Seasonal Coefficient of Performance
SH	Space heating
TANK	Storage tank

low as possible. This can be achieved by using a stratified storage tank [7], which requires accurate optimization in terms of volume and circulated flow rate [8,9]. On the other hand, the application of transcritical R744 heat pumps for SH production is constrained by the high return water temperatures, which result in significant throttling losses and a consequent decline in the overall system performance [10]. To address this issue, Wang et al. [11] proposed the integration of the heat pump with both radiator and floor radiant coil terminals for SH. Their results demonstrate seasonal performance (SCOP) improvement in the range 9–22 % compared to a system with only radiators. Another potential solution consists of using the R744 heat pump to satisfy both SH and DHW demands, as discussed in Artuso et al. [12]. Brodal and Jackson [13] conducted a numerical comparison between two heat pumps working with R744 and R410A for simultaneous SH and DHW production. The authors found that the R744 heat pump is able to outperform the R410A heat pump under certain operating conditions, specifically when the SH/DHW ratio is below 0.6–1 and the inlet water temperature at the gas-cooler is below 20 °C. Similarly, Zendehboudi [14] demonstrated that employing a R744 heat pump to simultaneously satisfy SH and DHW requirements, rather than DHW alone, can enhance the COP by up to 7.5 %, primarily due to lower discharge pressure and reduced pinch point temperature. Alternatively, in application with SH only, the adoption of an internal heat exchanger to decrease the refrigerant temperature before the throttling process can reduce the COP penalization [15,16].

Regarding the production of DHW using R290 heat pumps, Nawaz et al. [17] showed that a R290 heat pump is able to provide similar values of COP compared to the same system using R134a, when the water temperature lift is from 14 to 50 °C. However, in order to achieve high values of SCOP, high subcooling and proper dimensioning of storage tanks for DHW management have been identified as crucial factors [18]. Similar findings have been also reported by Ju et al. [19] when comparing two heat pumps for instantaneous DHW production working with R290 and R22. It is noteworthy that R290 can eventually lead to higher COPs when compared to R410A [20]. However, the optimal subcooling to maximize the performance, which depends on the temperature lift at the secondary fluid, has to be found [21]. It should be mentioned also the possibility of improving the efficiency of domestic R290 systems for DHW production by the introduction of an ejector [22].

It is noteworthy that only a few studies have employed numerical modelling to compare the performance of R744 and R290 heat pumps. Furthermore, the available data only covers DHW applications and often yields conflicting results. Tammaro et al. [23] developed a numerical model in TRNSYS16 to compare the seasonal COP of a 40 kW R744 and R290 air-to-water heat pump to produce DHW for hospital and school

applications under different climates. Interestingly, to achieve the same heating capacity when heating DHW from 10 °C to 60 °C, the R290 heat pump requires a compressor and a brazed plate heat exchanger condenser that are 2.5 and 3 times larger, respectively, than those of the R744 heat pump. Regarding SCOP, the R290 heat pump exhibits a reduction in energy consumption in warm and average climates, while the R290 and R744 systems have demonstrated comparable energy performance under cold climates. Similar findings have also been observed by Duarte et al. [24] for a direct expansion solar-assisted heat pump operating with a water temperature lift from 45 to 65 °C and by Masip et al. [25], who studied also the effect of different storage tanks. However, for water temperature lifts exceeding 25 K, R744 heat pumps may achieve a higher COP compared to R290 heat pumps [26,27].

From the literature review, it emerges that no studies have yet investigated the performance of R744 and R290 heat pumps for the simultaneous production of DHW and SH. This work addresses this gap by using a Matlab® numerical model (in which the results of the sub-model of each component have been validated) to size and evaluate the performance of different heat pumps. A key feature of the proposed model is its high flexibility, which enables the simulation of a wide range of heat pump configurations, such as the integration of multiple evaporators for exploiting different low thermal sources. Specifically, three heat pump systems operating with natural refrigerants are considered in this work: two using R744 and one using R290. The two R744 systems include an air-source heat pump (AHP) with a finned-coil heat exchanger as an evaporator and a dual-source solar-air heat pump (SAHP) equipped with a finned-coil and photovoltaic-thermal (PV-T) solar collectors as evaporators. The use of PV-T collectors as evaporators has been demonstrated to enhance the COP of the heat pump and to boost photovoltaic power production due to the cooling effect of the low-temperature refrigerant on the photovoltaic cells [28]. The R290 heat pump is an AHP with a finned-coil heat exchanger as an evaporator. A solar-assisted R290 configuration equivalent to the R744-SAHP has not been included so far due to the flammability of propane, which poses safety challenges and practical limitations in applications where refrigerants must circulate through PVT collectors. All three heat pumps are coupled to a single water storage tank, ensuring full coverage of the thermal demand for both DHW and SH without requiring any auxiliary heating source. The study compares the performance of these systems through two-day dynamic simulations and seasonal performance analyses under various SH and DHW demand profiles during winter in Rome (Italy) and Strasbourg (France).

2. Numerical model of the heating systems

2.1. System layout

A numerical model to simulate the performance of a heat pump (HP) and its hydronic circuits, for space heating and domestic hot water, has been developed. In the present work, three different heat pumps have been considered:

1) Air-source heat pump with R290 as refrigerant (R290-AHP).
2) Air-source heat pump with R744 as refrigerant (R744-AHP).
3) Dual-source solar-air heat pump with R744 as refrigerant (R744-SAHP).

Fig. 1 shows the layout of the heat pumps and their water circuits for SH and DHW production. The R290-AHP (see Fig. 1a) is equipped with a single-stage fixed speed ON/OFF reciprocating compressor (COMP), two brazed plate heat exchangers – one functioning as a condenser (COND) and the other as an internal heat exchanger (IHE) –, an electronic expansion valve (EEV), a finned coil heat exchanger as an air evaporator (FC-HE), and a low-pressure receiver (REC) installed between the FC-HE

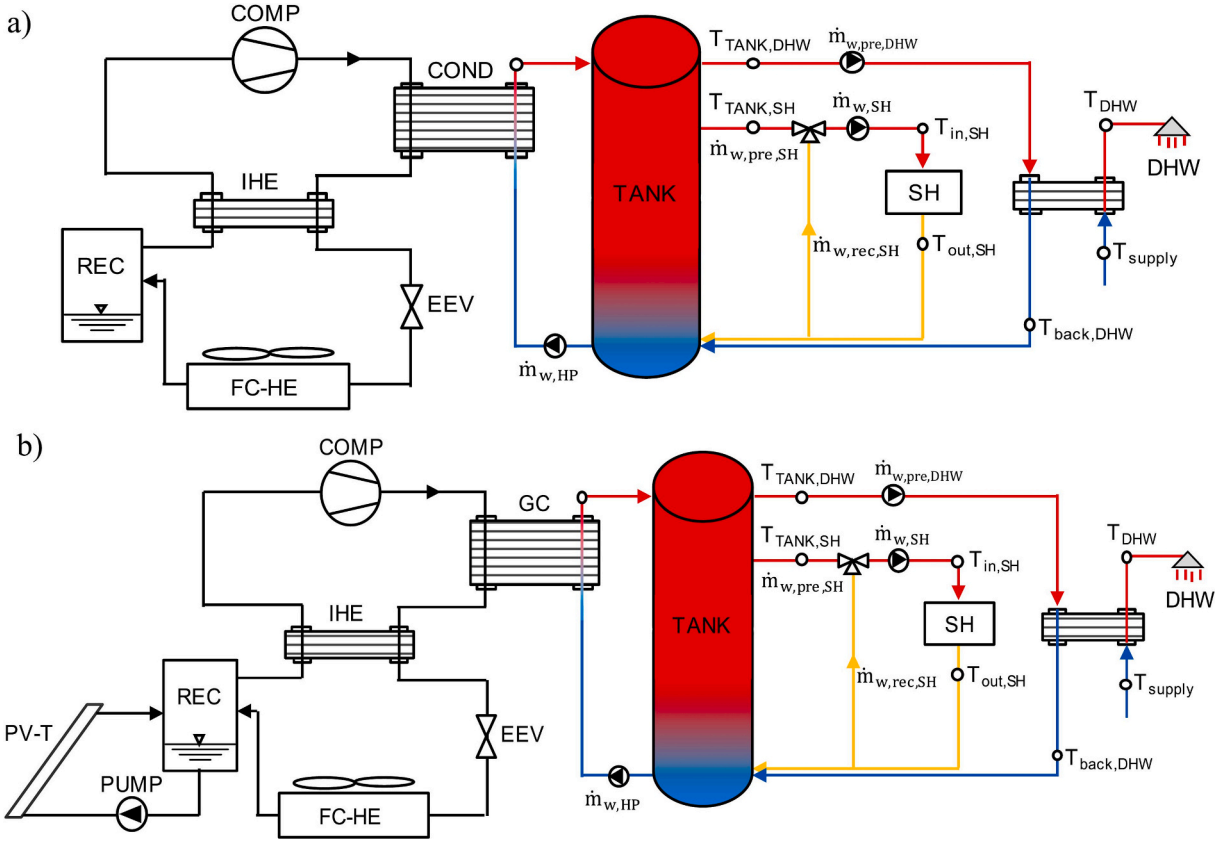

Fig. 1. a) Schematic of the refrigerant and water loops for the R290 heat pump. b) Schematic of the refrigerant and water loops for the solar-air R744 heat pump. For the R744 AHP heat pump, the configuration is that of b) without the PV-T circuit.

and the IHE. The R744-AHP and R744-SAHP are shown in a single scheme in Fig. 1b, and their layouts are similar to that of the R290-AHP. Since the critical temperature of carbon dioxide is equal to 31 °C, which is lower than the expected temperatures at the inlet of the heat pump during operation, the R744 cycle is transcritical. Therefore, in the R744-AHP (see Fig. 1b), the COND is replaced by a gas-cooler (GC). The R744-SAHP has a similar layout to the R744-AHP, with the addition of PV-T collectors as evaporators. The PV-T collectors operate as flooded evaporators and they are fed with liquid R744, which is drawn from the bottom of the REC by a circulating pump (PUMP). In this configuration, the solar and air evaporators work simultaneously, and the feasibility of this solution has been experimentally verified by Conte et al. [29]. After the electronic expansion valve, the R744 is vaporized in the air source evaporator and then enters the REC, from where the liquid is sent to the solar source evaporators. This configuration, enabling the use of both sources simultaneously, can run without the need for a control strategy to switch alternatively between the two evaporators. In the three heat pumps, the REC acts as a charge container that guarantees the presence of saturated vapor at the evaporator outlet (as discussed and experimentally verified in Zanetti et al. [30,31]). The IHE ensures a certain degree of superheating at the compressor suction for all three heat pumps considered.

In the two systems, the EEV operates differently depending on the refrigerant used. In the R290-AHP, it controls the subcooling at the outlet of the condenser, whereas in the R744-AHP and the R744-SAHP, it acts by controlling the high-pressure. Subcooling in the R290-AHP and high pressure in the R744-HPs are thus the parameters that can be optimized during the operations.

Regarding the water circuits depicted in Fig. 1, all three heat pumps considered in this work cover both the SH and DHW demands. The heat pumps are not directly connected to the user, but to an intermediate storage tank (TANK), which allows water to be tapped at the desired temperature due to the presence of thermal stratification. The use of a stratified thermal storage tank for SH applications is not common. However, in this system, the compressor operates at a fixed speed, which cannot be varied to directly match the load. Therefore, a storage tank is required to meet and overcome load fluctuations. The water circuit layout is the same for the three heat pump configurations. The water circuit consists of:

- One tank, which serves as the thermal storage for SH and DHW uses, similar to the combined storage tank used by Lee et al. [32].
- One pump circulates water from the bottom of the tank to the GC/COND, and then to the top of the tank.
- One pump extracts water from the middle of the tank and mixes it with a portion of the water flow returning from the SH system.
- One pump extracts water from the top of the tank and sends it to a heat exchanger to heat the DHW supply at the desired temperature.

2.2. Heat pump modelling

The two numerical models of the R290 and R744 heat pumps have been realized in Matlab® environment and slightly differ, due to the different layouts of the two heat pumps, as discussed in the previous section. Both models are based on the systematic resolution of the refrigerant thermodynamic cycle, where energy conservation equations are applied to each component. The common model inputs are the inlet/outlet water temperature at the GC/COND and the ambient conditions (air temperature and solar irradiance). Additional inputs are the subcooling at the outlet of the condenser, for the R290 heat pump, and the high-pressure at the gas-cooler, for the R744 heat pump. The model outputs are:

- The thermodynamic properties of the refrigerant along the vapor compression loop.
- The total power consumption of the heat pump (P_{tot}) includes the power consumed by the compressor, the fan of the finned coil evaporator, and the refrigerant PV-T circulation pump in the R744-SAHP system. The power consumption of the water loop pumps is not considered.
- The heating capacity (Q_{HP}) produced by the heat pump.
- The COP, defined as the ratio between the heating capacity and the total power consumption of the heat pump:

$$\mathrm{COP} = \frac{Q_{\mathrm{HP}}}{P_{tot}} \tag{1}$$

- The photovoltaic power production (P_{PV}).

The solution algorithm starts with the definition of first attempt values of the evaporation temperature and superheating at the compressor suction. The COMP sub-model calculates the refrigerant mass flow rate and the discharge enthalpy. Then, the sub-model of the GC/COND provides the refrigerant enthalpy at the outlet and the water mass flow rate. Subsequently, the IHE sub-model calculates a new value of superheating at the compressor inlet and enthalpy at the inlet of the EEV. Finally, the evaporator sub-model provides an updated value of the evaporation temperature. The cycle restarts from the COMP sub-model and repeats until convergence values of the evaporation temperature and superheating are obtained. This solution algorithm has already been used and validated against experimental data for the R744 single-source heat pump, operating with either air or solar energy as low temperature source, in previous work [31].

The following sections provide a detailed description of the modelling of the components, emphasizing its nature as a physical model rather than a black-box approach.

2.2.1. Brazed plate heat exchanger sub-model

In the brazed plate heat exchanger sub-models (COND, GC and IHE) a distributed parameters physical approach is adopted, where the volume of the channels is discretized into smaller elements, which are then treated as individual heat exchangers. In each element, the continuity and energy equations are solved. This approach has been fully described and validated in previous works in the case of a GC and IHE operating with R744 [28,29], and of a condenser operating with R32 [33].

This approach implies the estimation of the refrigerant side and water side heat transfer coefficients. The local heat transfer coefficients on the refrigerant side are calculated using the correlation of Longo et al. [34] for R290 condensation and of Zendehboudi et al. [35] for R744 gas-cooling. On the water side, the local heat transfer coefficient is calculated using the Martin correlation [36]. In the GC model, the iterative procedure allows to determine the temperature and enthalpy at the outlet of the heat exchanger given the high-pressure. In the COND model, the condensation pressure (and thus the condensation temperature) is varied through the iterative procedure and updated to obtain the desired refrigerant subcooled temperature.

The heating capacity provided by the heat pump Q_{HP} at the condenser or at the gas-cooler is calculated by the energy balance at the refrigerant side, knowing the difference between the inlet/outlet specific enthalpies and the mass flow rate.

$$Q_{\mathrm{HP}} = \dot{m}_r(h_{in} - h_{out}) \tag{2}$$

2.2.2. Finned coil sub-model

The finned coil evaporator consists of several copper tubes arranged in several multiple parallel circuits ($N_{circuits}$) attached to aluminum plain fins. The refrigerant flows inside the tubes and the air is forced outside by an electrical fan across the parallel fins and tubes, in a cross-flow configuration. The finned coil heat exchanger has been modelled using a distributed parameter approach, considering the three-dimensional heat and mass transfer, according to the work by Zanetti et al. [33].

The 3D discretization has been realized by dividing the heat exchanger volume into a certain number of rows (N_{rows}) and tubes per row (N_t), with each tube further discretized into N_d longitudinal segments. Therefore, the total number of elements j are:

$$N_j = N_{rows} N_t N_d \tag{3}$$

The main outputs of the model are the evaporation temperature and the outlet refrigerant enthalpy ($h_{out,\mathrm{FCHE}}$). The inputs of the model are:

- the refrigerant mass flow rate ($\dot{m}_r$);
- the refrigerant enthalpy at the inlet ($h_{in,\mathrm{FCHE}}$);
- the air mass flow rate ($\dot{m}_{air}$) and inlet temperature (T_{air});
- the desired superheating at the evaporator outlet.

Each element has a fixed length and it is analyzed as an independent heat exchanger, starting from the first element for which the input conditions are known. Following the refrigerant path, the inlet conditions of each subsequent element are calculated step by step, corresponding to the outlet conditions of the previous one.

The algorithm uses a guess-correct procedure where the evaporation temperature is first assumed. In the R744-ASHP and R290-ASHP models, the parameter used for the convergence criterion is the thermodynamic vapour quality at the outlet of the evaporator, which is calculated after each iteration and must be equal to 1, according to the heat pumps schematic in Fig. 1. In the R744-SAHP, the iterative procedure is performed after the PV-T submodel. For a better understanding, the algorithm is described below.

- The refrigerant mass flow rate is assumed to be equally distributed at the inlet of each of the $N_{circuits}$ circuits. For the steady-state continuity equation, the mass flow rate for each element ($\dot{m}_{r,j}$) is the same as the input of the corresponding circuit. Similarly, the air mass flow rate of each element ($\dot{m}_{air,j}$) is obtained by equally dividing the total mass flow rate by the total number of elements ($N_t\ N_d$):

$$\dot{m}_{r,j} = \frac{\dot{m}_r}{N_{circuits}} \tag{4}$$

$$\dot{m}_{air,j} = \frac{\dot{m}_{air}}{N_t\ \ N_d} \tag{5}$$

- The energy equation for a single discretization is solved using a guess value of the heat flow rate (Q_j):

$$h_{out,r,j} = \frac{Q_j}{\dot{m}_{r,j}} + h_{in,r,j} \tag{6}$$

Similarly, the outlet air enthalpy is calculated.

- The average thermodynamic properties of the fluids in the discretization are calculated. Refprop 10.0 [37] is used for the refrigerant properties, whereas the Kroger [38] equations are used for the moist air properties.
- Once the fluid properties and the heat flow rate are known, the product between the overall heat transfer coefficient (K) and the discretized area (A) is calculated. For a dry fin:

$$(KA)_{dry,i} = \frac{1}{\frac{1}{A_{int}\mathrm{HTC}_{r,j}} + \frac{\log\left(\frac{D_{ext}}{D_{int}}\right)}{2\pi\Delta L\lambda_t} + \frac{1}{A_{ext}\varepsilon_{fs,j}\mathrm{HTC}_{air,j}}} \tag{7}$$

where D, ΔL and A represent the tube diameter, the discretized length, and the heat transfer area (the subscripts "*ext*" and "*int*" refer to the external and internal side), λ_t is the tube thermal conductivity and $\varepsilon_{fs,j}$ is the fin surface efficiency calculated as:

$$\varepsilon_{fs,j} = 1 - \frac{A_f}{A_{ext}}(1 - \varepsilon_{f,j}) \tag{8}$$

where A_f is the surface of the fins and $\varepsilon_{f,j}$ is the fin efficiency calculated using the approximate solution of Schmidt [38].

For a wet fin, the overall heat transfer coefficient is calculated following the single potential method approach proposed by Threlkeld [39] and using the implementation of Kim and Bullard [40] adapted for a finned coil heat exchanger.

$$(KA)_{wet,i} = \frac{1}{\frac{b_{r,j}}{A_{int}\mathrm{HTC}_{r,j}} + b_{cond}\frac{\log\left(\frac{D_{ext}}{D_{int}}\right)}{2\pi\Delta L\lambda_t} + \frac{b_{film,j}}{A_{ext}\varepsilon_{fs-wet,j}\mathrm{HTC}_{air-wet,j}}} \tag{9}$$

Where the parameter b is the slope of air enthalpy as a function of temperature, $\varepsilon_{fs-wet,j}$ is the effectiveness of the wet fin [40] and $\mathrm{HTC}_{air-wet,j}$ is the heat transfer coefficient in wet conditions:

$$\mathrm{HTC}_{air-wet,j} = \frac{1}{\frac{cp_{air}}{b_{film}\mathrm{HTC}_{air,j}} + \frac{\delta_{film}}{\lambda_{film}}} \tag{10}$$

Where δ_{film} and λ_{film} are the thickness and thermal conductivity of the condensed water film.

- Once the overall heat transfer coefficient is known, the updated value of the heat flow rate (Q_j) is calculated for the *j-th* element using the ε-NTU method:

$$\varepsilon_j = \frac{Q_j}{Q_{max,j}} \tag{11}$$

Where $Q_{max,j}$ is the maximum heat flow rate in a perfect counter-current configuration and the value of the efficiency (ε_j) is calculated as a function of NTU and of the heat capacity ratio for a crossflow configuration.

- Once the new value of Q_j is calculated, the process is restarted from equation (6) until convergence is reached. Then the same algorithm is performed for the subsequent discretization until the end of the circuit length.
- At the end of the process, the calculated refrigerant enthalpy at the outlet of the heat exchanger is used to calculate the resulting thermodynamic vapor quality $x_{out,\mathrm{FCHE}}$. If $x_{out,\mathrm{FCHE}} > 1$, T_{evap} is increased, while, if $x_{out,\mathrm{FCHE}} < 1$, T_{evap} is decreased.

The refrigerant heat transfer coefficient ($\mathrm{HTC}_{r,j}$) used in equation (7) is calculated using various correlations, depending on the refrigerant conditions at the inlet of each element (pure evaporation, dry-out, and superheating). For each zone, specific correlations are used to estimate the heat transfer coefficient. In the pure evaporation zone, the Liu and Winterton correlation [41] is used. Regarding the dry-out zone, the transition criteria is reported in the study of Wojtan et al. [42]: for this region, a linear interpolation between the single and two-phase heat transfer coefficient is performed. In the single-phase region (superheating), the Gnielinski correlation [43] is used. Finally, the air-side heat transfer coefficient ($\mathrm{HTC}_{air,j}$) is calculated with the equation of Rich [44], whereas the air pressure drop is evaluated through the friction factor obtained with the Abu-Madi et al. [45] correlation in the case of dry fin and tube and that of Wang and Hihara [46] for wet fin and tube.

The model of the finned coil evaporator is here validated against experimental data collected with a prototype R744 heat pump installed at the Department of Industrial Engineering of the University of Padova and presented in Zanetti et al. [31]. The technical data of the finned coil heat exchanger equipped in the experimental system are reported in Table 1. Experimental measurements were conducted under steady-state conditions when the evaporating pressure remained within ± 0.2 bar

Table 1
Technical data of the real finned coil heat exchanger.

Finned coil		Fan	
Tube internal diameter	9.75 mm	Diameter	350 mm
Tube thickness	0.35 mm	N° of fan	1
Tube length	620 mm	Rotational speed	1400 rpm
N° of circuits	4	Air flow rate	2350 m^3/h
N° of tubes/rows	22 / 4	Power consumption	180 W
Tube spacing	25 mm	Variable speed	0 – 10 Vdc
Row spacing	21.65 mm		
Tube material	Copper		
Fin thickness	0.12 mm		
Fin spacing	3.2 mm		
Fin material	Aluminum		
Heat transfer area	15.3 m^2		

and the air temperature stayed within ± 1 K. Once the heat pump reached steady-state conditions, experimental data were recorded over 5 min at 10 s intervals, and the collected data points were subsequently averaged. The refrigerant pressure and temperature along the loop were monitored using pressure transducers (uncertainty of ± 5 kPa) and T-type thermocouples (uncertainty of ± 0.1 K), respectively. Air temperature was recorded using a RTD Pt-100 (uncertainty of ± 0.1 K). Specifically, the evaporation capacity of the finned coil evaporator is calculated by the energy balance at the refrigerant side ($Q_{evap} = \dot{m}_r \, \Delta h_{in\text{-}out}$), knowing the refrigerant mass flow rate and the specific enthalpy difference ($\Delta h_{in\text{-}out}$). The refrigerant specific enthalpies are estimated from temperature and pressure measurements using NIST Refprop 10.0 [37].

Fig. 2 shows the comparison between the numerical and the experimental evaporation capacity values in steady-state conditions during the following conditions: air temperature between 2.8 °C and 17.7 °C, air volumetric flow rate between 587.5 m^3/h and 2350 m^3/h, refrigerant mass flow rate between 7 g/s and 25 g/s, refrigerant vapor quality at the inlet between 0.1 and 0.4. The results suggest that the numerical model is able to estimate the evaporation capacity with an average and maximum percentage deviation equal to 4 % and 15 %, respectively.

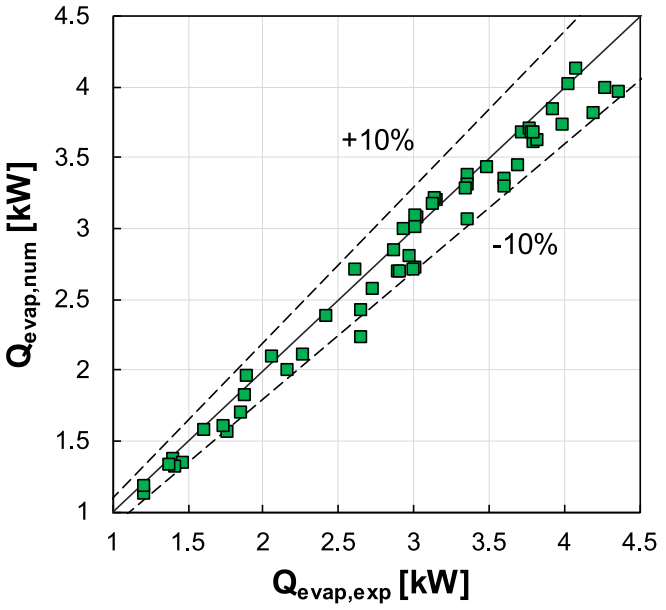

Fig. 2. Comparison between the numerical (num) and experimental (exp) values of the evaporation capacity in the finned coil evaporator of the R744 heat pump prototype analysed in Zanetti et al. [31]. Data refer to different steady-state conditions.

2.2.3. PV-T sub-model

The PV-T evaporator sub-model is based on the characteristic curve of the collector thermal efficiency as defined by the standard for solar thermal collectors [47].

$$\eta_{th} = a_1 \frac{T_{evap} - T_{air}}{G} + a_2 \tag{12}$$

where G is the solar irradiance on the tilted plane of the PV-T collector, while a_1 [W/(m^2 K)] and a_2 [-] are the coefficients. This methodology for defining the evaporation temperature in the PV-T evaporator has been validated by Zanetti et al. [31].

The electrical consumption of the CO_2 circulation pump was estimated from experimental data collected in Conte et al. [29]. The PV-T model accounts also for the electrical power produced by the PV modules:

$$P_{PV} = G \, A_{PV-T} \quad \eta_{PV} \tag{13}$$

where the electric conversion efficiency η_{PV} is defined by the standard for PV modules [48]:

$$\eta_{PV} = \eta_{STC} \quad (1 - \gamma \, (T_{cell} - 25)) \tag{14}$$

The cell temperature (T_{cell}) can be evaluated in presence or in absence of the cooling effect of the refrigerant:

$$T_{cell} = T_{air} + (\mathrm{NOCT} - 20) G / 800 \tag{15}$$

Parameters η_{STC} (electric conversion efficiency in standard conditions), γ (temperature coefficient) and NOCT (Nominal Operating Cell Temperature) are technical data of the PV module provided by the manufacturer.

2.2.4. Compressor sub-model

The compressor is modelled considering polynomial expressions for the electrical power consumption P_c and the mass flow rate processed $\dot{m}_r$, according to the standard for compressors [49]:

$$Y = C_1 + C_2 S + C_3 D + C_4 S^2 + C_5 SD + C_6 D^2 + C_7 S^3 + C_8 S^2 D + C_9 S D^2 + C_{10} D^3 \tag{16}$$

where the coefficient values have been obtained from the compressor manufacturer for R744 and R290 compressors, for a suction compressor superheating of 10 K. S corresponds to the evaporation temperature at the suction dew point (T_{evap} in [°C]) while D corresponds to the discharge pressure (p_{GC} in [bar]) for the R744 compressor and the condensing temperature at the discharge dew point (T_{COND} in [°C]) for the R290 compressor. To account for the suction compressor superheating, the mass flow rate can be corrected with the density ratio:

$$\dot{m}_r = \frac{\rho_{suction}}{\rho_{10K}} \, \dot{m}_{r,10K} \tag{17}$$

where the subscript 10 K refers to 10 K suction compressor superheating condition. A change of superheat has a negligible impact on the power consumption of the compressor, as suggested by the AHRI standard 540 [50].

2.3. Water circuit model

2.3.1. Storage tank sub-model

In the literature, stratified water storage tanks have been modelled with different methods [51,52]. In this work, to develop the model of the water storage tank, the heat transfer is considered based on heat conduction and convection between layers, with an approach similar to that described in other studies [53,54]. The tank is divided into n layers along its height, each representing a node, as shown in Fig. 3a. Each i-th

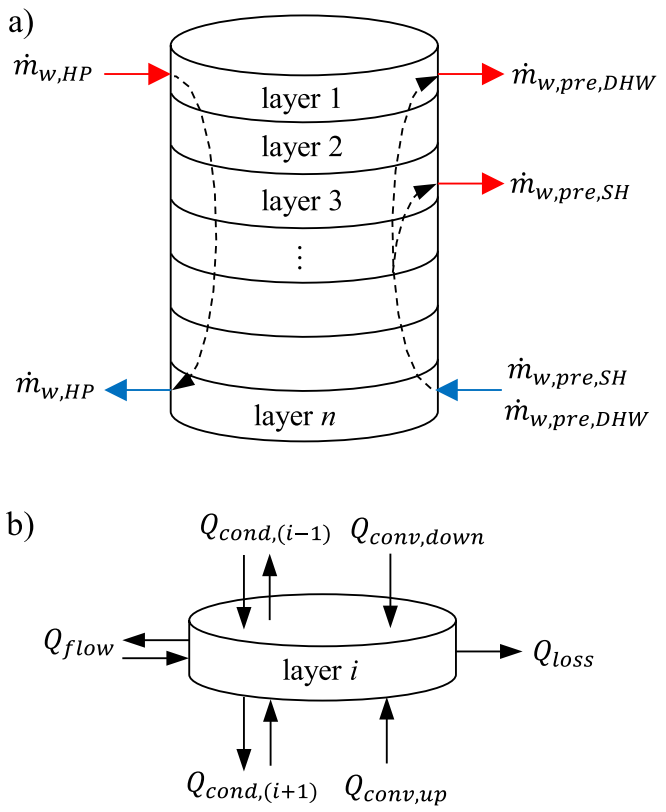

Fig. 3. a) schematic of the layer division in the water storage tank and b) heat fluxes for a generic$i$-th layer.

layer can exchange heat and mass with the upper (i - 1) and lower ($i + 1$) layers. The heat transfer along the radial direction of the tank is neglected, therefore the temperature inside each layer is uniform and only the heat transfer along the flow direction was considered. For each layer, the mass flow rate on the upper (i - 1) and lower ($i + 1$) layer ($\dot{m}_{w,i}$) can be defined as the sum of the contributions of the water mass flow rate from the heat pump ($\dot{m}_{w,\mathrm{HP}}$) and the water mass flow rate drawn for SH ($\dot{m}_{w,pre,\mathrm{SH}}$) and DHW ($\dot{m}_{w,\mathrm{DHW}}$).

$$\dot{m}_{w,i} = \dot{m}_{w,\mathrm{HP}} + \dot{m}_{w,pre,\mathrm{SH}} + \dot{m}_{w,\mathrm{DHW}} \tag{18}$$

In particular, as shown in Fig. 3a, $\dot{m}_{w,\mathrm{HP}}$ flows in a downward direction and is assumed to have a positive value. Conversely, $\dot{m}_{w,pre,\mathrm{SH}}$ and $\dot{m}_{w,\mathrm{DHW}}$ flow in an upward direction and are assigned negative values. Therefore, if $\dot{m}_{w,i} > 0$, the flow is downwards. Conversely, if $\dot{m}_{w,i} < 0$, the flow is upwards.

Fig. 3b illustrates the heat fluxes in the i-th layer. The heat balance is described by the following equations:

$$\rho V c_p \frac{\mathrm{d}T}{\mathrm{d}t} = Q_{flow} + Q_{cond} + Q_{conv} - Q_{loss} \tag{19}$$

where ρ and c_p are the density and the specific heat capacity of water in the layer, and V is the volume of the layer. Q_{flow} represents the advective term accounting for the water mass entering or exiting the layer from the inlet/outlet ports. This term only applies to the tank layers where water inflows and outflows occur in Fig. 3a, namely layer 1 (incoming flow from the heat pump and the outgoing flow to the DHW circuit), layer 3 (outgoing flow to the SH circuit), and layer n (incoming flows from the SH and DHW circuits and outgoing flow to the heat pump). Q_{flow} calculation depends on the corresponding mass flow rate and water temperature:

$$Q_{flow} = \sum \dot{m}_{w,flow} c_p T_{flow} \tag{20}$$

The Q_{cond} is the resulting heat flow rate from the conduction heat transfer between layer (i) and the upper (i - 1) and lower (i + 1) layers:

$$Q_{cond} = Q_{cond,(i-1)} + Q_{cond,(i+1)} \tag{21}$$

$$Q_{cond,(i-1)} = \lambda\ A_i\ (T_{i-1} - T_i)/H_i \tag{22}$$

$$Q_{cond,(i+1)} = \lambda\ A_i\ \ (T_{i+1} - T_i)/H_i \tag{23}$$

where A_i and H_i represent the cross-sectional area and the height of the layer, respectively.

Q_{conv} is the advective term accounting for the mass inflows and outflows in the layer, resulting from the net mass flow ($\dot{m}_i$). Depending on the direction, it can be expressed as:

$$Q_{conv,down} = \dot{m}_{w,i}\ c_p\ (T_{i-1} - T_i) \tag{24}$$

$$Q_{conv,up} = \dot{m}_{w,i}\ \ c_p\ (T_i - T_{i+1}) \tag{25}$$

Q_{loss} accounts for the heat losses due to conduction in the wall of the tank between the water and the outside. For a cylindrical geometry with diameter D, it can be expressed as:

$$Q_{loss} = \frac{2\pi\lambda_{wall}\ H_i\ (T_i - T_{amb})}{ln\left(\frac{D/2+l_{wall}}{D/2}\right)} \tag{26}$$

where λ_{wall} and l_{wall} are the thermal conductivity and the thickness of the cylinder wall, respectively.

2.3.2. SH system sub-model

The SH system layout is designed and modelled to guarantee defined inlet ($T_{in,\mathrm{SH}}$) and outlet ($T_{out,\mathrm{SH}}$) temperatures for the SH (see Fig. 1) when a thermal load (Q_{SH}) is required. Therefore, the water flow rate $\dot{m}_{w,\mathrm{SH}}$ to satisfy the SH load is calculated as:

$$\dot{m}_{w,\mathrm{SH}} = \frac{Q_{\mathrm{SH}}}{c_p\left(T_{in,\mathrm{SH}} - T_{out,\mathrm{SH}}\right)} \tag{27}$$

If the temperature ($T_{\mathrm{TANK,SH}}$) of the mass flow rate drawn from the tank ($\dot{m}_{w,pre,\mathrm{SH}}$) is higher than the required temperature $T_{in,\mathrm{SH}}$, $\dot{m}_{w,pre,\mathrm{SH}}$ is mixed with a fraction of the water flow coming back from the user ($\dot{m}_{w,rec,\mathrm{SH}}$), which is at the temperature $T_{out,\mathrm{SH}} < T_{in,\mathrm{SH}}$. The value of $\dot{m}_{w,pre,\mathrm{SH}}$ is calculated by solving the following energy and mass equations.

$$\dot{m}_{w,\mathrm{SH}}\ c_p\ T_{in,\mathrm{SH}} = \dot{m}_{w,pre,\mathrm{SH}}\ c_p\ T_{\mathrm{TANK,SH}} + \dot{m}_{w,rec,\mathrm{SH}}\ c_p\ T_{out,\mathrm{SH}} \tag{28}$$

$$\dot{m}_{w,pre,\mathrm{SH}} = \dot{m}_{w,\mathrm{SH}} - \dot{m}_{w,rec,\mathrm{SH}} \tag{29}$$

2.3.3. DHW system model

The DHW system layout is designed and modelled to ensure water heating from the supply temperature (T_{supply}) to a defined DHW temperature (T_{DHW}) in a secondary heat exchanger (see Fig. 1), when a specific water flow rate ($\dot{m}_{w,\mathrm{DHW}}$) is required. The required DHW thermal load (Q_{DHW}) is defined as:

$$Q_{\mathrm{DHW}} = \dot{m}_{w,\mathrm{DHW}}\ c_p\ \left(T_{\mathrm{DHW}} - T_{supply}\right) \tag{30}$$

To calculate the water flow rate ($\dot{m}_{w,pre,\mathrm{DHW}}$) drawn from the tank, a fixed temperature difference between T_{supply} and the temperature at the outlet of the heat exchanger coming back to the tank ($T_{back,\mathrm{DHW}}$) has been assumed.

$$\dot{m}_{w,pre,\mathrm{DHW}} = \frac{Q_{\mathrm{DHW}}}{c_p\left(T_{\mathrm{TANK,DHW}} - T_{back,\mathrm{DHW}}\right)} \tag{31}$$

It must be noted that, the heat transfer losses to the environment from water pipes, refrigerant discharge line, condenser/gas cooler and heat exchanger for DHW are neglected.

3. Definition of the case study

In this section, the sizing of the three heat pumps and the corresponding hydronic circuit for seasonal simulations is presented. The thermal loads for SH and DHW are also defined for two locations taken under examination (Rome and Strasbourg). Finally, the input parameters and system regulation strategies for the simulations are discussed.

3.1. Heat pump design

The sizing procedure for R744-AHP and R290-AHP involves selecting the COMP size (displacement), GC/COND heat transfer area (number of plates), and the finned coil evaporator heat transfer area (number of circuits, tube length, and number of fans). In addition, the R744-SAHP design involves selecting the number of PV-T collectors.

The GC and COND brazed plate heat exchangers use 379 mm × 79 mm plates according to commercially available solutions (such as those installed in the previous works [28,29,31]). The compressor for the two different refrigerants was identified based on the design heat pump capacity, using the Frascold S.p.A. selection software of single-stage reciprocating compressors [55], which also provides the coefficients to be used in Eq. (15). To evaluate the specific compressor work, a compressor electric efficiency of 0.95 has been assumed. The geometry of the finned coil evaporator and the fan type have been assumed to be the same as the ones investigated in the previous studies [28,29,31], whose technical data are reported in Table 1. For a single fan, a fixed air mass flow rate of 1727 m^3/h and an electrical consumption of 79 W have been considered, corresponding to the operation at 75 % of the maximum speed. During the design process, the appropriate number of circuits, tube length, and number of fans of the finned coil evaporator were carefully selected.

The technical data of the PV-T collectors were assumed to be identical to those tested in Zanetti et al. [31]. In particular, the dimensions of each PV-T collector are 1.650 × 0.992 m^2. According to the producer datasheet, the nominal electric power is 270 W, η_{STC} is 0.165, γ is equal to 0.0041 and the NOCT is 48 °C. When the CO_2 flows in the heat exchanger of the PV-T evaporators, the NOCT is modified to account for the cooling effect on the PV cells. A mean value equal to 24 °C has been assumed according to the measurements reported in Zanetti et al. [31]. The effect of the PV cell cooling leads to an increase of about 1 % in the electrical conversion efficiency when the cell temperature is reduced from 48 °C (NOCT producer datasheet) to 24 °C.

The thermal efficiency coefficients in Eq. (10) were obtained experimentally from the data collected in a previous work [30]: a_1 = -16.553 and a_2 = 0.4149. The collectors are considered to be south-facing with a tilt angle of 45°.

The three heat pumps have been designed to work with a nominal heating capacity of 15 kW at the design conditions. The design conditions are: outside ambient temperature equal to 7 °C, water temperature at the GC/COND inlet equal to 10 °C and at the outlet equal to 60 °C.

The IHE was not taken into account in the design process. It has been considered a brazed plate heat exchanger with 4 plates of 377 mm × 120 mm, after verifying that it always provides at least 10 K superheating at the compressor suction.

Some additional conditions have been imposed for the single heat pumps, only for the design:

- For the R290-AHP, a fixed subcooling of 40 K inside the condenser has been imposed in order to enhance the heat pump performance. This high subcooling value was selected based on the experimental data of Pitarch et al. [56], who identified it as the optimal value for maximizing the COP in an R290 heat pump working under similar operating conditions (with water inlet and outlet temperature at the heat sink of 10 °C and 60 °C, respectively).
- For the R744-AHP and R744-SAHP, a fixed high-pressure value of 90 bar has been imposed.
- For the R744-SAHP, a solar irradiance equal to 350 W/m^2 was assumed.

First, the R290-AHP and the R744-AHP were designed. The heat exchangers have been sized to get the same temperature difference between the outside ambient and refrigerant evaporating temperatures (ΔT_{evap} = 8.5 K) and between GC/COND refrigerant outlet and water inlet temperatures (ΔT_{COND} = 4.5 K), in agreement with the study of Tammaro et al. [23]. Pressure drops are neglected in the GC/COND and evaporators. Furthermore, a compressor suction superheating of 9 K has been fixed. The size of the components was determined through multiple iterations of the numerical model of the heat pump until the ΔT_{evap} and ΔT_{COND} values were similar for both heat pumps, with a maximum deviation of 0.5 K.

Then, the R744-SAHP was considered to be equipped with the same sized components as the R744-AHP, with the addition of the PV-T collectors. Under this assumption, the R744–SAHP can achieve the nominal heating capacity even when solar radiation is not available, i.e. when the

Table 2
Design results of the three heat pumps.

Component	Properties	Units	R290-AHP	R744-AHP	R744-SAHP
Compressor	Model		D3-15.1AXH	D4-3TK	D4-3TK
	Number of pistons	–	2	2	2
	Displacement	m^3/h	15.36	3.00	3.00
	Speed	rpm	1450	1450	1450
	Consumption	kW	3.58	3.72	3.52
Gas-cooler/ Condenser	Number of plates	–	65	38	38
	Area	m^2	1.75	1.02	1.02
	ΔT_{COND} (design)	K	4.52	4.26	8.30
	KA (design)	W/K	1356	999	937
	Capacity (design)	kW	15.14	15.01	15.77
Evaporator	Type		Finned coil	Finned coil	Finned coil+ PV-T
	Tube length	m	2	1.7	1.7
	Number of circuits	–	6	6	6
	Number of fans	–	3	3	3
	Fans consumption	kW	0.24	0.24	0.24
	KA (design)	W/K	1492	1273	1335
	Number of PV-T	–	0	0	11
	PV-T area	m^2	0	0	11.44
	ΔT_{evap} (design)	K	8.98	8.64	5.59
	Capacity (design)	kW	11.56	11.50	12.24
Heat pump	COP (design)	–	3.97	4.01	4.19

PV-T collectors do not work as an evaporator. The number of PV-T collectors has been chosen to produce approximately 3 kW of electrical power, under standard test conditions (STC). This value corresponds to a typical small photovoltaic system installation in center of Italy [57].

Table 2 shows the results of the design process of the three heat pumps (R290-AHP, R744-AHP and R744-SAHP), highlighting the main characteristics of the compressor, gas-cooler/condenser, and evaporator. Due to the lower volumetric cooling capacity of R290 compared to R744 for the same evaporation temperature (volumetric latent heat of vaporization is approximately 3880 kJ/m^3 for R290 and 22550 kJ/m^3 for R744), the displacement of the R290-AHP compressor is five times larger than that of the compressor used in the R744 heat pumps. Despite having the same nominal heating capacity, the R290-AHP requires a condenser with a higher number of plates (resulting in a larger heat transfer area) compared to the gas-cooler used in the R744 heat pumps. Compared to the R744-AHP, the R744-SAHP exhibits a lower ΔT_{evap} value due to the increased evaporation area provided by the additional 11 PV-T evaporators. This expanded area raises the evaporation temperature and reduces the compressor power consumption, leading to a higher COP.

The COP values under the design conditions are 3.97 for the R290-AHP, 4.01 for the R744-AHP, and 4.19 for the R744-SAHP. Notably, the R290-AHP and R744-AHP achieve comparable COPs.

3.2. Water storage tank design

The capacity of the storage tank is a crucial factor in the heat pump systems' ability to meet both SH and DHW demands. The size of the tank determines the amount of heat that can be stored, which depends on the mass flow rate of the water and its temperature level. Delivering heat at the correct temperature for the desired application is essential considering also that the user comfort level is defined as the ratio of hours in which the system meets thermal demands to the total number of hours in the given period. This study aims to develop a system that guarantees 100 % comfort without relying on an external auxiliary heater. Therefore, the storage tank functions as a thermal buffer, enhancing system flexibility. In the event of sudden demand spikes, the tank must have enough water at the required temperature to meet the demand.

The selected water tank has a capacity of 700 L and a height of 2 m, with a height-to-diameter ratio equal to 3 to maintain temperature stratification. This tank size is comparable to the 750 L proposed by Lee et al. [32]. The tank is insulated with a 0.05 m thick layer of material that has a thermal conductivity of 0.02 W/(m K). At the beginning of the simulation, the water temperature inside the tank is set at 20 °C. The storage tank is divided into 20 layers. The incoming water line from the heat pump and the outgoing DHW line are connected to layer 1, located at the top of the tank. The outgoing SH line is connected to layer 3. The returns of DHW and SH lines, as well as the water line to the heat pump, are located at the bottom part of the tank (layer 20).

3.3. SH and DHW thermal loads

Two distinct locations, Rome and Strasbourg, have been chosen to represent the SH load under both mild and cold climate conditions, respectively. The Test Reference Year data for these locations has been

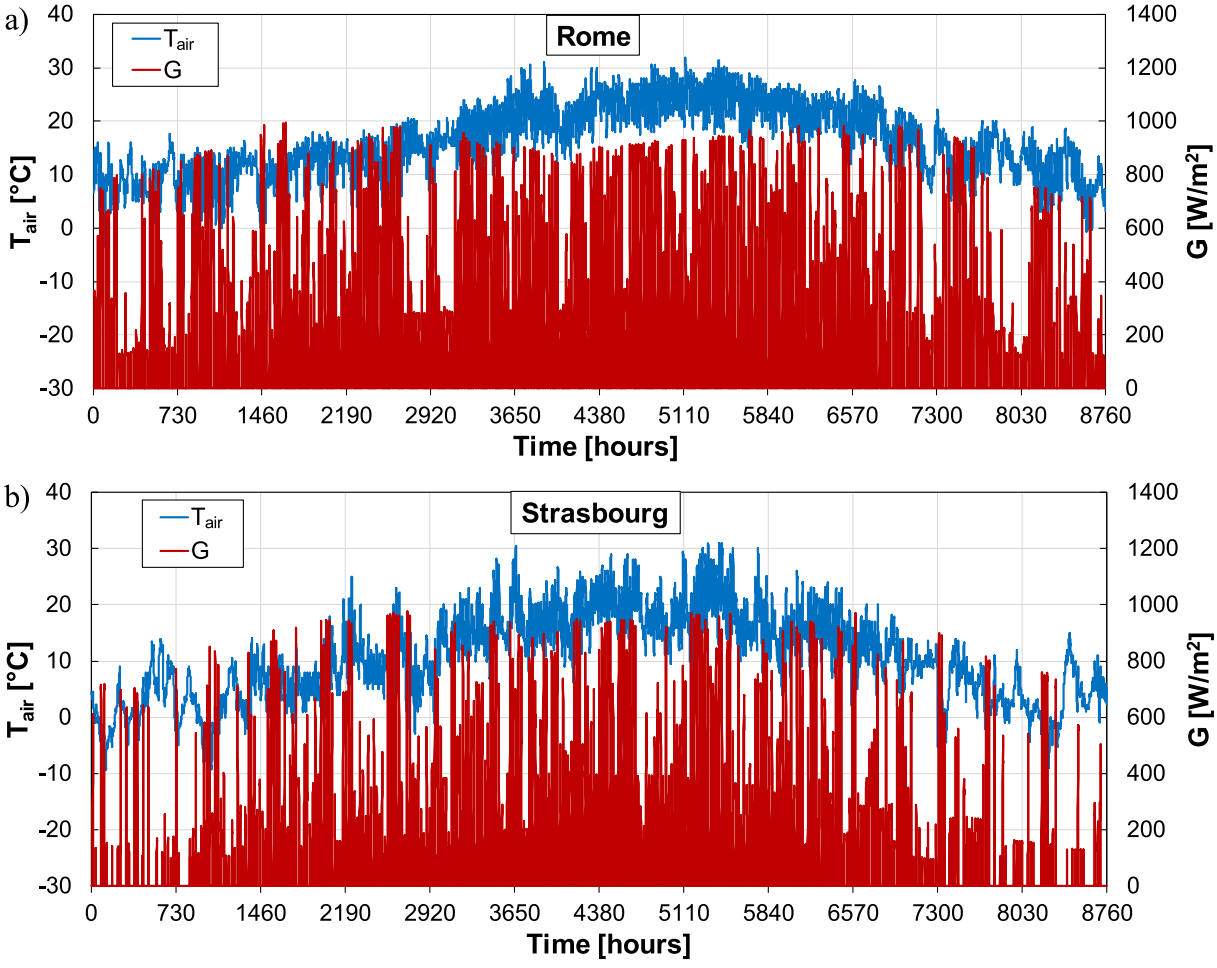

Fig. 4. Annual air temperature (T_{air}) and global irradiance on the tilted plane (G) in a) Rome and b) Strasbourg.

obtained from the Energyplus® database [58] and the hourly data of air temperature (T_{air}) and global irradiance on the tilted plane of the PV-T collectors (G) are plotted for the two cities in Fig. 4.

The seasonal simulations do not cover the entire year, but only the heating season of each location. For Rome, the heating season is from November 1st to April 15th (166 days), and during this period, the minimum and the average air temperature are −4.0 °C and 10.2 °C, respectively, while the maximum and the average solar irradiance are 1000 W/m^2 and 410 W/m^2, respectively. For Strasbourg, the heating season is from October 1st to May 15th (227 days), and during this period, the minimum and the average air temperature are −9.6 °C and 4.6 °C, respectively, while the maximum and the average solar irradiance on the tilted plane are 1000 W/m^2 and 320 W/m^2, respectively.

The SH load profile of the simulated building was derived from a linear equation as a function of outdoor air temperature, which is the same for the two locations. A maximum SH load of 10 kW is imposed at an air temperature of −10 °C, while the SH load is 0 kW at 18 °C. Thus, no heating demand is present when the outdoor air temperature is above 18 °C. It has been assumed that the SH load is required during daylight hours, from 7 am to 10 pm, thus there is no SH load demand during the night hours. The total seasonal hours of SH load are 2415.5 for Rome and 3277 for Strasbourg. The seasonal SH demand requirement in Rome is 5837 kWh, which averages 35.2 kWh per day, while in Strasbourg is 13,574 kWh, which averages 59.8 kWh per day.

The DHW demand of the simulated building is the same for the locations selected. Two different discretized DHW load profiles were considered with 5-minute intervals.

The first load profile (DHW#1) is given with two different load distributions for weekdays (from Monday to Friday) and weekends (Saturday and Sunday), as shown in Fig. 5. The load was assumed to be active only during the daytime, between 7:00 am to 10:00 pm, in alignment with the SH load profile. On weekdays (Fig. 5a), the DHW demand is concentrated in three time zones: early morning, lunchtime, and evening. On the other hand, on weekends (Fig. 5b), the DHW demand is more evenly distributed throughout the day. For annual simulations, the weekly DHW load profile was repeated uniformly across the year. This load profile corresponds to a typical DHW consumption for a residential building [59].

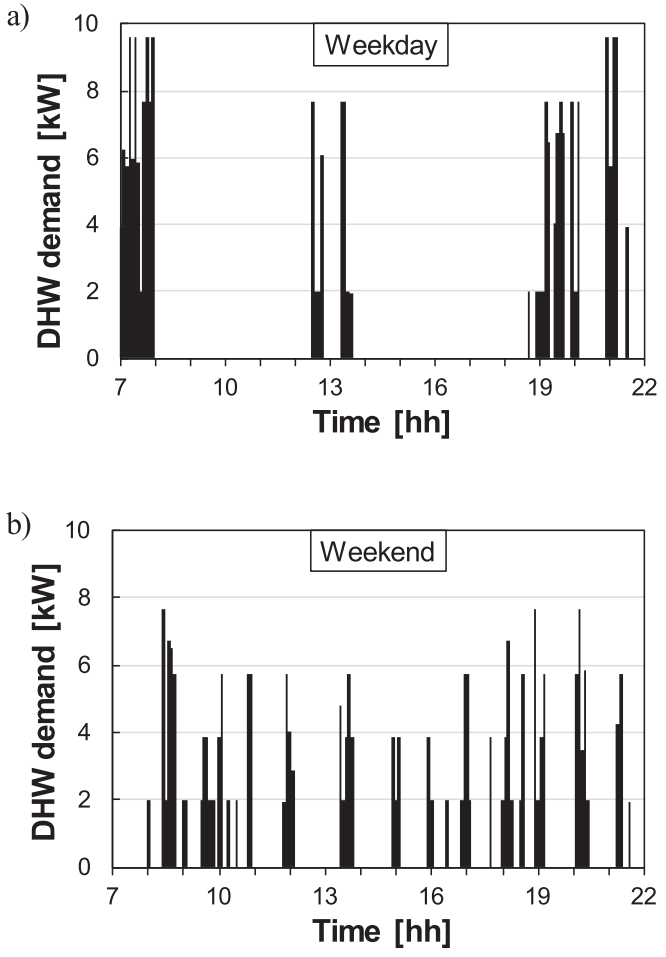

Fig. 5. a) DHW#1 load for a) weekday. b) DHW#1 load for weekend.

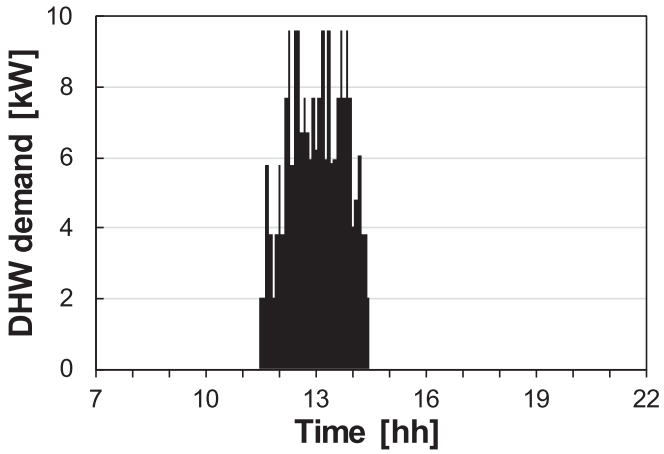

Fig. 6. DHW#2 load for a day.

The second load profile (DHW#2) is given with a unique load profile distribution for all days of the season, as shown in Fig. 6. In comparison to DHW#1, the DHW demand for DHW#2 corresponds to the same values required by the DHW#1 profile for the weekday but distributed over the central hours of the day, from 11:30 to 14:30. This load profile corresponds to a typical DHW consumption for a canteen [60].

Both profiles have an average daily DHW load of 18.65 kWh during the heating season. Therefore, the seasonal DHW demand in Rome amounts to 3096 kWh (equivalent to 50 % of the SH load), with a total of 598.5 seasonal hours for DHW#1 and 498 seasonal hours for DHW#2. In Strasbourg, the seasonal demand is 4233 kWh (equivalent to 30 % of the SH load), corresponding to 820.2 seasonal hours for DHW#1 and 681 seasonal hours for DHW#2.

3.4. System input parameters and regulation strategy

The following conditions are set for the operations of the hydronic loop:

- T_{DHW} and T_{supply} (see Fig. 1) are set to 50 °C and 10 °C, respectively.
- The temperature difference between T_{supply} and $T_{back,DHW}$ (see Fig. 1) is fixed at 1 K.
- For domestic heating, a floor heating system with water flowing from 35 °C ($T_{in,SH}$) to 30 °C ($T_{out,SH}$) has been considered.

The heat pumps always produce hot water at 60 °C and work with a constant compressor speed of 50 Hz. The compressor's ON/OFF cycling is regulated based on the temperature measured at a specific layer inside the tank, ensuring the desired temperature level is consistently maintained for the user. The sensor positions were determined through an optimization process. Specifically:

- The compressor turns ON when the temperature sensor located at 90 % of the tank's height from the bottom (layer 2) measures a water temperature below 55 °C, or when the temperature sensor located at 10 % of the tank's height from the bottom (layer 18) gauges a water temperature below 30 °C. These two sensors are the DHW and SH temperature controller, respectively. This dual-sensor system

maintains proper stratification within the tank and prevents the lower section from becoming too cold, which is crucial for meeting peak hot water demands without engaging the auxiliary resistance heater.

- The compressor switches OFF when a temperature of 35 °C is reached at 10 % of the tank's height from the bottom (layer 18), to avoid high water temperatures at the inlet of the heat pump. The balance between the mass flow rate of hot water supplied by the heat pump and the returning cold water from the user's circuit is critical for maintaining the system's efficiency. The predominance of cold water entering from the bottom can result in hot water accumulating at the top of the tank. Consequently, the strategic placement of the temperature sensor is essential. If the sensor position is too low, the heat pump may activate too frequently, increasing power consumption and consequently reducing the SCOP. Conversely, if the sensor is placed too high, the heat pump may not engage often enough, failing to heat an adequate volume of water. This can lead to discomfort for the user due to an insufficient hot water supply.

In the gas-cooler, the high pressure is not set at a constant value, but it is optimized with an iterative procedure: at each time step the COP is calculated for a range of high pressure between 80 to 100 bar, and the value of pressure resulting in the highest COP is selected as the operating pressure. A similar procedure is implemented to optimize the subcooling in the condenser by selecting a value of subcooling within the range of 5–40 K.

The simulation time-step is fixed to 1 min.

4. Results and discussion

Heating seasonal simulations were conducted to examine three combinations of load demand coupling, as previously defined:

1) SH: only SH demand, with no DHW demand.
2) SH + DHW: simultaneous demand for both SH and DHW.
3) DHW: only DHW demand, with no SH demand.

For the DHW load, the two profiles described in Sec. 3.4 were considered: DHW#1 and DHW#2. The input parameters are the same for all simulations. Additionally, to analyze the effect of PV cell cooling on the electrical power produced by the PV-T collectors in the R744-SAHP, it was chosen to couple the R290-AHP and the R744-AHP with an equivalent number of photovoltaic panels, without PV cells cooling.

4.1. Dynamic response of the heat pumps

First, to better understand the operation of the three heat pumps under varying environmental conditions and heating load profiles, two-day dynamic simulations are analyzed for Rome.

4.1.1. Heat load with DHW#1 profile

Fig. 7 displays the results of the numerical simulation conducted over two consecutive days (7th and 8th January) in Rome in the presence of a combined SH + DHW#1 load: a weekday (*day1*) and a weekend day (*day2*). The environmental conditions, including T_{air} and G, varied over the two days (Fig. 7a). *Day1* had a higher T_{air} (average of 7 °C) and lower G (maximum 340 W/m^2) compared to *day2*, which is characterized by an average T_{air} of 3 °C and a maximum G equal to 790 W/m^2. As shown in Fig. 7b, the required SH load varies depending on T_{air} for the two days: a maximum of 5.4 kW for *day1* and 6.6 kW for *day2*. In contrast, the DHW load has a different distribution depending on the day of the week, as explained in Sec. 3.4, with a maximum of 9.6 kW for *day1* and 7.7 kW for *day2*.

Fig. 7c-d show the heating production (Q_{HP}) and the electrical power consumption (P_{tot}) of the three heat pumps. The R290-AHP always produces a higher Q_{HP} (approximately 1–2 kW) with slightly increased energy consumption P_{tot} (by about 0.1–0.2 kW) compared to the two R744 heat pumps, even though all systems were required to meet the same thermal energy demand over the two days (172.2 kWh in total). This demonstrates the best instantaneous performance of the R290-AHP. As a result, the R290-AHP operates for fewer hours over the two days, specifically 12 h and 10 min, compared to the 14 h of the R744-SAHP and the 14 h and 40 min of the R744-AHP. In addition, the results predict that all the heat pumps perform four on/off cycles well distributed during one day. On the other hand, when analyzing energy fluxes, the R290-AHP produces 172.2 kWh of thermal energy with an energy consumption of 48.1 kWh. In comparison, the R744-AHP and R744-SAHP demonstrate both higher thermal energy production (3.9 % and 5.2 %, respectively) and higher electric energy consumption (18.1 % and 14.5 %, respectively).

When comparing the two R744 heat pumps, it is evident that R744-SAHP produces slightly higher Q_{HP} (about 0.5 kW) and requires almost the same P_{tot} in the absence of solar radiation. In contrast, when considering the solar radiation (e.g. from 12:00 to 14:00 on *day2*), the R744-SAHP increases the Q_{HP} by 1.5 kW compared to the R744-AHP, due to the increased availability of the heat source energy. This is also reflected in the trend of the evaporating temperature shown in Fig. 7e (in this graph, no values are shown when the compressor is off). The T_{evap} for the R744-SAHP is slightly higher (approximately 1–2 K) than that of the R744-AHP under conditions without solar radiation. This is attributed to the larger heat transfer area of the R744-SAHP evaporator, consisting of both the finned coil and the PV-T collectors. When G increases, T_{evap} rises further by about 3–4 K due to the significant contribution of the solar radiation in the PV-T collectors.

The interaction between heat pumps and photovoltaic systems is also analyzed. Table 3 presents the main simulation results, including the total operating hours of the heat pump (HP_{on}), the operating hours of the heat pump during solar radiation availability ($HP_{on,G}$), the ratio of these two values, the total energy consumption of the heat pump (E_{tot}), the energy produced by the photovoltaic system (E_{PV}), and the energy self-consumed by the system (E_{self}), defined as the energy produced by the photovoltaic system that is directly consumed by the heat pump during its operation. Regardless of the type of heat pump, the total operating hours were higher on *day2* compared to *day1*, due to the higher thermal load demand. This trend is also evident in the operating hours of the heat pump under solar radiation, which accounted for approximately 20 % of the total on *day1* and 30 % on *day2*. During these periods, the photovoltaic system was also active, generating electricity. For all three considered systems, the heat pump was able to self-consume approximately 20 % of the photovoltaic energy produced on *day1* and 43 % on *day2*, without a dedicated battery energy storage.

These preliminary results suggest that all three heat pumps operate during periods of higher thermal load demand. Therefore, their performance is strongly influenced by the thermal load distribution throughout the day, and this is typically associated with conditions of lower thermal source availability. For instance, when the thermal load demand is more concentrated in the early and late hours of the day, the lowest air temperatures and reduced or absent solar radiation would penalize the performance of the AHPs and limit the benefits of using the SAHP.

To assess how the performance of the heat pumps depends on the thermal load distribution, the simulation presented in Fig. 7 was repeated, substituting the DHW#1 profile with the DHW#2 profile.

4.1.2. Heat load with DHW#2 profile

The inputs and results corresponding to the DHW#2 profile are shown in Fig. 8 and Table 4. Similar to the results of the previous simulation reported in Fig. 7, the R290-AHP achieves the highest values of Q_{HP} and P_{tot}, followed by the R744-SAHP and the R744-AHP. The key difference lies in the distribution of the DHW load, which is concentrated from 11:30 to 14:30. As shown in Table 4, over the 12 h of solar radiation across the two days, the heat pumps operate for different

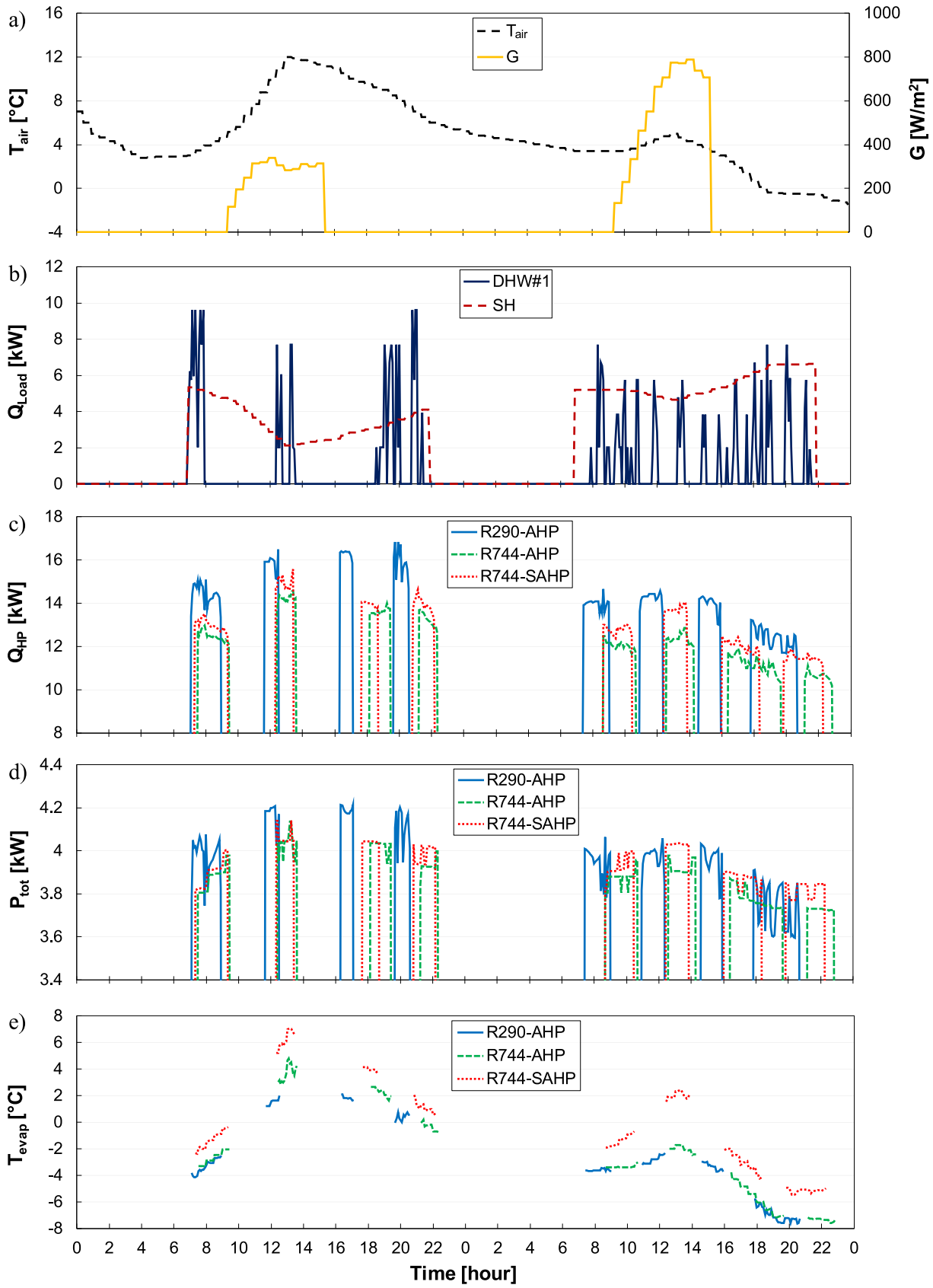

Fig. 7. Simulations results over two consecutive days considering SH + DHW#1 load in Rome for the three different heat pumps (R290-AHP, R744-AHP, R744-SAHP). a) Air temperature and solar irradiance; b) thermal loads; c) heating capacity produced; d) power consumption; e) evaporation temperature.

Table 3
Working hours and electric energy produced and consumed during the simulations over two consecutive days considering SH + DHW#1 load in Rome for the three different heat pumps.

SH + DHW#1		HP_{on} [h:min]	$HP_{on,G}$ [h:min]	$\frac{HP_{on,G}}{HP_{on}}$ [%]	E_{tot} [kWh]	E_{PV} [kWh]	E_{self} [kWh]	$\frac{E_{self}}{E_{PV}}$ [%]
R290-AHP	day1	4:40	0:55	19.6 %	19.0	5.7	1.0	18.0 %
	day2	7:30	2:25	32.2 %	29.0	11.4	4.9	43.2 %
	Total	12:10	3:20	27.4 %	48.1	17.0	5.9	34.8 %
R744-AHP	day1	5:45	1:15	21.7 %	22.7	5.7	1.2	22.0 %
	day2	8:55	3:00	33.6 %	34.0	11.4	5.3	46.4 %
	Total	14:40	4:15	29.0 %	56.8	17.0	6.5	38.3 %
R744-SAHP	day1	5:45	1:10	20.3 %	22.9	5.7	1.2	21.3 %
	day2	8:15	2:30	30.3 %	32.1	11.7	4.6	39.3 %
	Total	14:00	3:40	26.2 %	55.0	17.4	5.8	33.4 %

durations: 4 h and 50 min for the R290-AHP (39 % of the total operating hours), 7 h and 30 min for the R744-AHP (57 % of the total operating hours), and 6 h and 45 min for R744-SAHP (50 % of the total operating hours).

Table 4 also reports the heat pump energy consumption, the photovoltaic energy production, and the energy self-consumed by the system. Although the photovoltaic energy production remains unchanged for the R290-AHP and R744-AHP systems compared to the previous case with DHW#1 load profile, a 2 % increase is observed with the R744-SAHP. This increase is attributed to improved cell cooling, resulting from the extended operating time of the heat pump during these hours. Compared to the simulations with the DHW#1 profile, the percentage of energy self-consumed over the total energy production with the DHW#2 profile has increased. On *day1*, this percentage reaches 35 % for R290-AHP, 43 % for R744-AHP, and 39 % for R744-SAHP. On the sunnier *day2*, with higher thermal demand, these values rise to 60 % for R290-AHP, 77 % for R744-AHP, and 70 % for R744-SAHP.

Based on the previous simulations, the results presented in Table 3 and Table 4 demonstrate increased photovoltaic energy production (E_{PV}) for R744-SAHP compared to the two AHPs. This improvement is attributed to the cooling effect of the evaporating R744 on the PV-T collectors, which enhances the electric conversion efficiency. This effect is particularly pronounced on *day2* (8th of January), when solar irradiance is higher. On this day, the photovoltaic energy production for the two AHPs is 11.4 kWh, whereas coupling the PV-T with the R744-SAHP yields 11.7 kWh under DH + DHW#1 load and 11.9 kWh under DH + DHW#2 load, corresponding to increases of 2.5 % and 4.7 %, respectively.

These results stress the crucial impact of the distribution of the thermal load profile on both the performance of the heat pump and the photovoltaic energy production for the R744-SAHP. To explore this further, the dynamic profile of photovoltaic power production by the PV modules on *day2* was analysed. Fig. 9 shows the instantaneous photovoltaic power production for *day2* under DH + DHW#1 load (Fig. 9a) and DH + DHW#2 load (Fig. 9b). It compares PV modules without cooling (P_{PV}), paired with AHPs, and PV-T collectors of the R744-SAHP (P_{PVT}). Yellow-shaded areas represent periods when the R744-SAHP is operating. Generally, there is no significant difference between the instantaneous production of electricity (respectively P_{PV} and P_{PVT}) until midday. This happens for two reasons. Firstly, when the R744-SAHP is turned off, the PV-T collectors work as PV modules without cooling. Secondly, the low solar irradiance value doesn't allow for a significant increase in photovoltaic power production when the R744-SAHP is turned on. However, in the afternoon, P_{PVT} is approximately 7–8 % higher than P_{PV}. This improvement coincides with the operation of the heat pump works during periods with high solar irradiance (grey-shaded area). The longer operating time of the heat pump under the DH + DHW#2 load (from 12:15 to 15:00 in Fig. 9b) compared to the DH + DHW#1 load (from 12:25 to 13:50 in Fig. 9a) explains the higher photovoltaic energy production observed.

4.2. Seasonal performance

The performance of the systems during the heating season is compared in terms of SCOP, defined as the ratio of the total heating energy produced by the heat pump (E_{HP}) to the total electric energy consumption of the heat pump (E_{tot}). This encompasses the consumption of the compressor, the fan, and the pump to feed the PV-T collectors:

$$SCOP = \frac{E_{HP}}{E_{tot}} = \frac{\sum Q_{HP}\ time}{\sum P_{tot}\ time} \tag{32}$$

4.2.1. Heat load with DHW#1 profile

Fig. 10 compares the SCOP values of the three heat pumps under the three different thermal load conditions (SH only, SH + DHW#1, and DHW#1 only) for the two climatic conditions in Rome (a) and Strasbourg (b). Table 5 and Table 6 report the main results of the seasonal simulations for the two locations.

Fig. 10 shows that the highest SCOP is consistently achieved with the R290-AHP, while the lowest is with the R744-AHP, regardless of the thermal load or location. The SCOP values for the R744-AHP are, respectively, 3.31, 3.51, and 3.98 for SH, SH + DHW#1, and DHW#1 loads in Rome, and 3.01, 3.16, and 3.70 in Strasbourg. These values are lower in Strasbourg due to the colder average winter temperature, which results in a lower heating capacity, and thus a longer operation time of the heat pump, necessary to cover the required heating load. Compared to the R744-AHP, the R290-AHP SCOP is 14.0 %, 11.3 %, and 4.6 % higher in the case of Rome, and 15.2 %, 13.1 %, and 5.4 % in the case of Strasbourg for SH, SH + DHW#1, and DHW#1 loads, respectively. In addition, the R744-SAHP shows a higher SCOP compared to the R744-AHP, due to the higher thermal source availability at the evaporator. In particular, the SCOP increases of 4.0 %, 4.1 %, and 4.5 % in Rome, and 4.2 %, 4.1 %, and 4.0 % in Strasbourg for SH, SH + DHW#1, and DHW#1 loads, respectively. These increases in SCOP are more significant in Rome due to the typically higher number of sunny days with higher solar irradiance during the heating season, compared to Strasbourg. Additionally, all the results suggest that when the share of DHW load relative to SH load increases, the SCOP of all three heat pumps improves. However, this increase is more pronounced for the R744 heat pumps (about 20 %) compared to the R290 heat pump (about 10 %). It is interesting to note that the SCOP of the R744-SAHP is comparable to that of the R290-AHP when only DHW#1 is required.

Taking into consideration each thermal load, the rise in SCOP is not related to an increase in the thermal energy generated by the heat pump (E_{HP} in Table 5 and Table 6), as they all produce the same heating during the season, but rather to a reduction in electrical consumption. As shown by E_{tot} in Table 5 for Rome, the R290-AHP consumes approximately 12.3 % less for SH, 10.1 % less for SH + DHW#1, and 4.3 % less for DHW#1 compared to the R744-AHP. Similar values are shown in Table 6 for Strasbourg, where the consumptions are reduced by 13.1 %, 11.9 %, and 5.0 % for SH, SH + DHW#1, and DHW#1 loads, respectively. The electricity consumption is lower in Rome than in Strasbourg

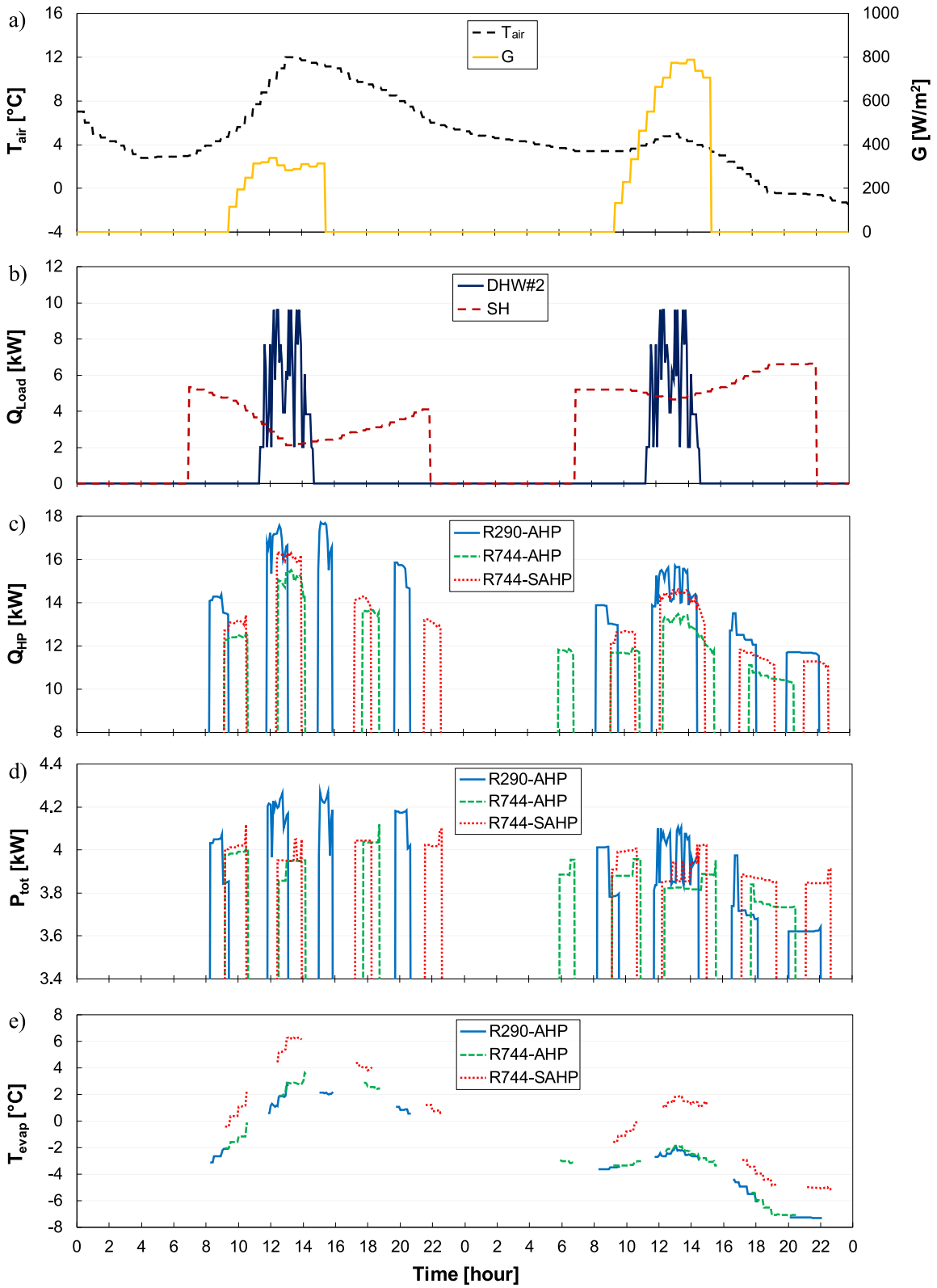

Fig. 8. Simulations results over two consecutive days considering SH + DHW#2 load in Rome for the three different heat pumps (R290-AHP, R744-AHP, R744-SAHP). a) Air temperature and solar irradiance; b) thermal loads; c) heating capacity produced; d) power consumption; e) evaporation temperature.

due to the shorter heating period and the higher air temperature.

The values of electrical energy produced by the PV modules (E_{PV}) is also reported in Table 5 and Table 6. The use of PV-T in the R744-SAHP, which directly cools down the cells employing the evaporating refrigerant results in a slightly higher electrical energy production compared to the use of uncooled PV modules: an increase of 0.6 %, 0.9 %, and 0.4 % in Rome, and 1.0 %, 1.2 %, and 0.4 % in Strasbourg for SH, SH + DHW#1, and DHW#1 loads are found respectively. This electrical energy production increase is rather limited, and this is because PV-T collectors work as PV modules without subcooling when the heat

Table 4
Working hours and electric energy produced and consumed during the simulations over two consecutive days considering SH + DHW#2 load in Rome for the three different heat pumps.

SH + DHW#2		HP_{on} [h:min]	$HP_{on,G}$ [h:min]	$\frac{HP_{on,G}}{HP_{on}}$ [%]	E_{tot} [kWh]	E_{PV} [kWh]	E_{self} [kWh]	$\frac{E_{self}}{E_{PV}}$ [%]
R290-AHP	day1	4:30	1:50	40.7 %	18.5	5.7	2.0	34.6 %
	day2	8:00	3:00	37.5 %	30.6	11.4	6.8	60.0 %
	Total	12:30	4:50	38.7 %	49.1	17.0	8.8	51.6 %
R744-AHP	day1	4:20	2:55	67.3 %	17.2	5.7	2.4	42.9 %
	day2	8:55	4:35	51.4 %	34.2	11.4	8.8	76.9 %
	Total	13:15	7:30	56.6 %	51.4	17.0	11.2	65.6 %
R744-SAHP	day1	5:10	2:40	51.6 %	20.7	5.7	2.2	39.3 %
	day2	8:15	4:05	49.5 %	32.2	11.9	8.4	70.4 %
	Total	13:25	6:45	50.3 %	52.9	17.6	10.6	60.3 %

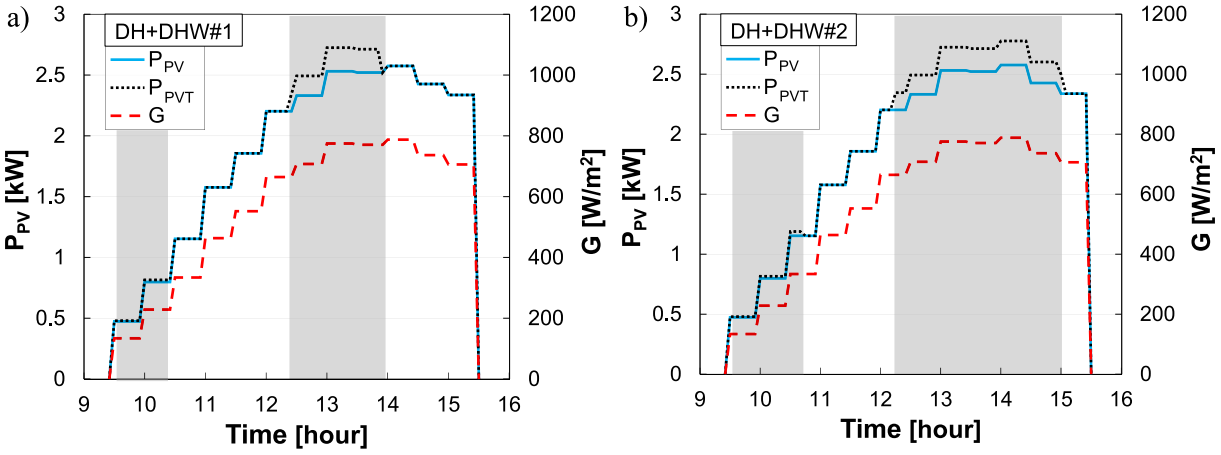

Fig. 9. Photovoltaic power production during the simulated *day2* in Rome, comparing PV modules without cooling (P_{PV}) and PV-T collectors (P_{PVT}) under two scenarios: a) DH + DHW#1 load and b) DH + DHW#2 load. Solar irradiance on the tilted plane is also reported. Grey-shaded areas indicate periods when the R744-SAHP is on.

pump turns off. In fact, during the heating season in Rome, the PV system operates for approximately 1189 h, while the operation in PV-T mode is limited to 169 h in SH (14 % of the total hours), 199 h in SH + DHW#1 (17 % of the total hours), and 68 h in DHW#1 (6 % of the total hours). The same consideration can be drawn for the simulations in Strasbourg, but here the total seasonal PV-T working hours are higher due to the longer heating season and this explains the higher energy production compared to Rome. In particular, the PV system operates for approximately 1305 h, while the operation in PV-T mode is limited to 319 h in SH (24 % of the total hours), 378 h in SH + DHW (29 % of the total hours), and 84 h in DHW (6 % of the total hours). Considering the energy self-consumed reported in Table 5 for Rome, the two R744 heat pumps can self-consume more energy compared to the R290-AHP. Generally, the energy self-consumed corresponds to 13 % of the photovoltaic production in the case of SH load, 16 % for SH + DHW#1 load, and 6.5 % for DHW#1 load. Similar consideration can be made for Strasbourg results (Table 6), but the percentage of the energy self-consumed on the photovoltaic production increases, corresponding to approximately 22 % for SH load, 26 % for SH + DHW#1 load, and 7 % for DHW#1 load.

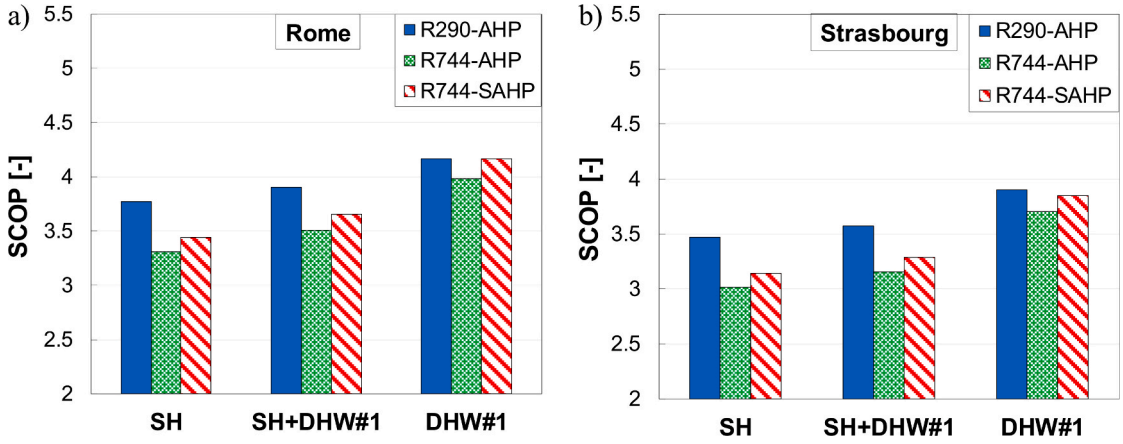

Fig. 10. SCOP of the three heat pumps (R290-AHP, R744-AHP, R744-SAHP) in the case of SH load only, SH + DHW#1 load, and DHW#1 load only for a) Rome and b) Strasbourg locations.

Table 5
Results of the seasonal simulations in Rome in terms of SCOP, thermal energy production (E_{HP}), total energy consumption (E_{tot}), photovoltaic energy production (E_{PV}), and energy self-consumed (E_{self}).

Load	Heat pump	SCOP [-]	E_{HP} [kWh]	E_{tot} [kWh]	E_{PV} [kWh]	E_{self} [kWh]	$\frac{E_{self}}{E_{PV}}$ [%]
SH	R290-AHP	3.77	6014	1594	1582	185	11.7 %
	R744-AHP	3.31	6015	1817	1582	209	13.2 %
	R744-SAHP	3.44	6014	1747	1592	207	13.0 %
SH + DHW#1	R290-AHP	3.90	9125	2337	1582	230	14.6 %
	R744-AHP	3.51	9123	2599	1582	266	16.8 %
	R744-SAHP	3.65	9124	2497	1596	259	16.3 %
DHW#1	R290-AHP	4.17	3311	794	1582	97	6.2 %
	R744-AHP	3.98	3308	830	1582	107	6.8 %
	R744-SAHP	4.16	3310	795	1588	104	6.5 %

Table 6
Results of the seasonal simulation in Strasbourg in terms of SCOP, thermal energy production (E_{HP}), total energy consumption (E_{tot}), photovoltaic energy production (E_{PV}), and energy self-consumed (E_{self}).

Load	Heat pump	SCOP [-]	E_{HP} [kWh]	E_{tot} [kWh]	E_{PV} [kWh]	E_{self} [kWh]	$\frac{E_{self}}{E_{PV}}$ [%]
SH	R290-AHP	3.47	13,790	3975	1483	300	20.2 %
	R744-AHP	3.01	13,784	4573	1483	361	24.3 %
	R744-SAHP	3.14	13,797	4391	1497	336	22.4 %
SH + DHW#1	R290-AHP	3.57	18,025	5053	1483	360	24.3 %
	R744-AHP	3.16	18,004	5733	1483	421	28.4 %
	R744-SAHP	3.29	18,020	5497	1500	401	26.7 %
DHW#1	R290-AHP	3.90	4519	1159	1483	98	6.6 %
	R744-AHP	3.70	4515	1220	1483	108	7.3 %
	R744-SAHP	3.85	4517	1174	1488	103	6.9 %

4.2.2. Heat load with DHW#2 profile

Similarly to the previous simulations, Fig. 11 shows the SCOP values of the heat pumps under the three different thermal load conditions (SH only, SH + DHW#2, and DHW#2 only) for Rome (a) and Strasbourg (b) climates. The results for SH load are the same as previously presented in 4.2.2. Compared to the seasonal performance of the system with DHW#1 profile (Fig. 10), the characteristics of the DHW#2 load improve the SCOP of all three heat pumps. In particular, for SH +

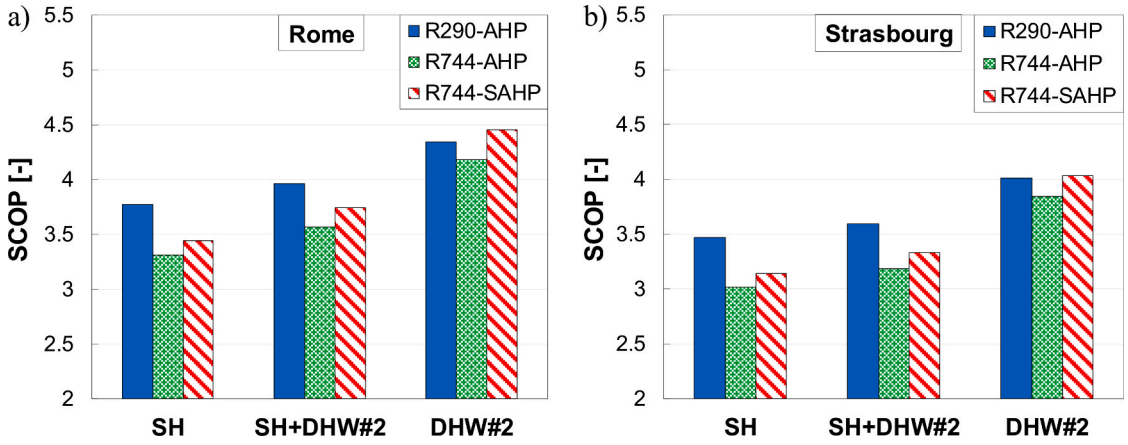

Fig. 11. SCOP of the three heat pumps during SH load only, SH + DHW#2 load, and DHW#2 load only for a) Rome and b) Strasbourg locations.

Table 7
Results of the seasonal simulation in Rome regarding SCOP, thermal energy production (E_{HP}), total energy consumption (E_{tot}), photovoltaic energy production (E_{PV}), and energy self-consumed (E_{self}). Results for SH load are reported in Table 5.

Load	Heat pump	SCOP [-]	E_{HP} [kWh]	E_{tot} [kWh]	E_{PV} [kWh]	E_{self} [kWh]	$\frac{E_{self}}{E_{PV}}$ [%]
SH + DHW#2	R290-AHP	3.96	9125	2301	1582	461	29.1 %
	R744-AHP	3.57	9116	2555	1582	515	32.6 %
	R744-SAHP	3.74	9118	2437	1609	489	30.4 %
DHW#2	R290-AHP	4.35	3315	763	1582	279	17.7 %
	R744-AHP	4.18	3310	792	1582	298	18.9 %
	R744-SAHP	4.45	3315	745	1600	296	18.5 %

Table 8
Results of the seasonal simulation in Strasbourg regarding SCOP, thermal energy production (E_{HP}), total energy consumption (E_{tot}), photovoltaic energy production (E_{PV}), and energy self-consumed (E_{self}). Results for SH load are reported in Table 6.

Load	Heat pump	SCOP	E_{HP}	E_{tot}	E_{PV}	E_{self}	$\frac{E_{self}}{E_{PV}}$
		[-]	[kWh]	[kWh]	[kWh]	[kWh]	[%]
SH + DHW#2	R290-AHP	3.60	18,022	5026	1483	569	38.4 %
	R744-AHP	3.19	17,954	5703	1483	655	44.2 %
	R744-SAHP	3.33	18,009	5432	1513	633	41.8 %
DHW#2	R290-AHP	4.01	4521	1128	1483	277	18.7 %
	R744-AHP	3.84	4521	1176	1483	301	20.3 %
	R744-SAHP	4.03	4514	1120	1497	285	19.0 %

DHW#2 load, the R290-AHP achieves again the highest SCOP for Rome and Strasbourg, 3.96 and 3.60 respectively, compared to the 3.57 and 3.19 of the R744-AHP, and the 3.74 and 3.33 of the R744-SAHP. On the contrary, for DHW#2 load only, the R744-SAHP achieves the highest SCOP for Rome and Strasbourg, 4.45 and 4.03 respectively, compared to the 4.18 and 3.84 of the R744-AHP and the 4.35 and 4.01 of the R290-AHP.

Table 7 and Table 8 report the main results of the seasonal simulations for Rome and Strasbourg, respectively, with the DHW#2 load. Compared to the simulations with DHW#1, the thermal energy generated by the heat pump (E_{HP}) is almost the same, while the electric consumption is lower in a range between 1 % to 6 %. This explains the higher SCOP achieved by the heat pumps when the DHW#2 profile is considered instead of the DHW#1 profile.

Photovoltaic energy production remains constant regardless of whether the R290-AHP or R744-AHP is employed or different thermal loads are used. This consistency is due to the photovoltaic conversion efficiency being independent of the operation of the system. However, with the R744-SAHP, photovoltaic production increases by approximately 1 % compared to the case with DHW#1, as a result of the enhanced operation of the heat pump during periods of solar radiation.

The self-consumption doubles compared with the simulations with DHW#1, for all three heat pumps, regardless of the locations. In particular, the percentage of the self-consumed energy on the photovoltaic production in Rome (Table 7) increases approximately by 30 % for the SH + DHW#2 load, and 7 % for the DHW#2 load. While for Strasbourg (Table 8), this percentage increases by about 40 % for the SH + DHW#2 load, and 20 % for the DHW#2 load. These results indicate that load imbalances occurring in the middle of the day promote greater self-consumed electricity within the system.

In conclusion, the results of Figs. 10-11 indicate that, for space heating applications, the propane-based heat pump outperforms the CO_2-based system, even when considering the use of air and solar evaporators operating simultaneously. In contrast, when considering the domestic hot water production, the performance of the two heat pumps, one using R290 and the other using R744, is comparable.

5. Conclusions

This paper presents a numerical analysis of the seasonal performance of three heat pump systems employing two natural refrigerants, R290 and R744, for space heating and domestic hot water production during the winter season in two reference locations: Rome and Strasbourg. The systems under investigation include a R290 air-source heat pump (R290-AHP), a R744 air-source heat pump (R744-AHP), and a R744 dual-source solar-air heat pump (R744-SAHP). In the R744-SAHP, a conventional finned coil operates simultaneously with PV-T collectors as evaporators. The numerical model simulates the thermodynamic behavior of each system component as well as the hydronic circuit. Three thermal loads were analyzed: combined space heating and domestic hot water production (SH + DHW), space heating only (SH-only), and domestic hot water only (DHW-only). Two distinct DHW load profiles were analyzed: one representing a typical consumption profile of a residential building (DHW#1) and the other corresponding to a canteen consumption profile (DHW#2).

The main results of the study are:

- The COP values under the design conditions are 3.97 for the R290-AHP, 4.01 for the R744-AHP, and 4.19 for the R744-SAHP. Notably, the R290-AHP and R744-AHP achieve comparable COPs.
- Dynamic simulations indicate that the performance of all three heat pump systems is highly sensitive to the temporal distribution of the thermal load over the day. In particular, when the demand is concentrated in the early morning and late evening hours (as in the DHW#1 profile) system performance is negatively affected due to lower ambient air temperatures and minimal or absent solar radiation. Conversely, when the thermal demand aligns with daylight hours (as in the DHW#2 profile) higher evaporating temperatures are achieved, and the R744-SAHP benefits more significantly from solar energy input. Moreover, the thermal load profile also impacts the self-consumption of electricity generated by the PV panels. In Rome, self-consumption increases from 6–17 % under the DHW#1 profile to 18–33 % under DHW#2. In Strasbourg, the increase is even more pronounced, rising from 7–28 % under DHW#1 to 19–44 % under DHW#2.
- The SCOP values for the R290-AHP range from 3.47 to 4.01 in Strasbourg and 3.77 to 4.35 in Rome, depending on the thermal load combination. The R744-AHP SCOP ranges from 3.01 to 3.84 in Strasbourg and 3.31 to 4.18 in Rome, while the R744-SAHP SCOP ranges from 3.14 to 4.03 in Strasbourg and 3.44 to 4.45 in Rome. Regardless of the thermal load or location, the highest SCOP is consistently achieved with the R290-AHP, while the lowest is realized with the R744-AHP.
- Despite R290 in small heat pump systems for SH and DHW can lead to energy savings, the condenser must be sized to have a sufficient number of plates (larger heat transfer area compared to R744 heat pumps). However, since most of the refrigerant charge is present in the condenser, higher volumes would mean a higher refrigerant charge.
- An increase in the SCOP of approximately 4 % was observed for the R744-SAHP compared to the R744-AHP. This performance enhancement is attributed to the simultaneous utilization of both air and solar energy sources, which leads to a higher evaporating temperature at the same ambient air conditions relative to the R744-AHP. To better exploit the advantages of the solar source, it is beneficial to run the system during daylight hours and to pair it with a large thermal storage system to effectively manage the loads.

Declaration of competing interest

The authors declare that they have no known competing financial interests or personal relationships that could have appeared to influence the work reported in this paper.

Acknowledgements

Financial support by the European Commission - Next Generation EU, Missione 4, Componente C2 Investimento 1.1 "Fondo per il Programma Nazionale di Ricerca e Progetti di Rilevante Interesse Nazionale (PRIN 2022 PNRR)", CUP C53D23008240001, "Next generation inverse cycles using CO2 based mixtures as refrigerant (CO2MIX)", project code: P2022C494T.

Data availability

Data will be made available on request.

References

[1] IEA, Heating, Paris, 2024. www.iea.org/reports/heating.
[2] IEA, The Future of Heat Pumps, Paris, 2022. www.iea.org/reports/the-future-of-heat-pumps.
[3] EU No 2024/573, Regulation (EU) 2024/573 of the European Parliament and of the Council of 7 February 2024 on fluorinated greenhouse gases, amending Directive (EU) 2019/1937 and repealing Regulation (EU) No 517/2014, Off. J. Eur. Union (2024).
[4] H. Wang, Z. Ji, C. Wang, Z. Zhu, Y. Wang, H. Lin, Experimental study of propane heat pump system with secondary loop and vapor injection for electric vehicle application in cold climate, Appl. Therm. Eng. 217 (2022) 119196, https://doi.org/10.1016/J.APPLTHERMALENG.2022.119196.
[5] D. Wu, B. Hu, R.Z. Wang, Vapor compression heat pumps with pure low-GWP refrigerants, Renew. Sustain. Energy Rev. 138 (2021) 110571, https://doi.org/10.1016/J.RSER.2020.110571.
[6] E. Granryd, Hydrocarbons as refrigerants—an overview, Int. J. Refrig 24 (2001) 15–24, https://doi.org/10.1016/S0140-7007(00)00065-7.
[7] S. Smitt, I. Tolstorebrov, A. Hafner, Performance improvement of integrated CO_2 systems with HVAC and hot water for hotels, Therm. Sci. Eng. Prog. 23 (2021) 100869, https://doi.org/10.1016/j.tsep.2021.100869.
[8] M. Dongellini, C. Naldi, G.L. Morini, Influence of the hydronic loop configuration on the energy performance of a CO_2 heat pump for domestic hot water production in a multi-family building, Building Simulation Conf. Proceed. (2022) 3228–3235, https://doi.org/10.26868/25222708.2021.30700.
[9] F.J.S. Velasco, M.R. Haddouche, F. Illán-Gómez, J.R. García-Cascales, Experimental characterization of the coupling and heating performance of a CO2 water-to-water heat pump and a water storage tank for domestic hot water production system, Energ. Buildings 265 (2022) 112085, https://doi.org/10.1016/j.enbuild.2022.112085.
[10] Y. Wang, Z. Ye, X. Yin, Y. Song, F. Cao, Energy, exergy and exergoeconomic evaluation of the air source transcritical CO_2 heat pump with internal heat exchanger for space heating, Int. J. Refrig. 130 (2021) 14–26, https://doi.org/10.1016/j.ijrefrig.2021.06.028.
[11] Z. Wang, G. Li, F. Wang, Y. Zhang, Performance investigation of a transcritical CO2 heat pump combined with the terminal of radiator and floor radiant coil for space heating in different climates, China, J. Build. Eng. 44 (2021) 102927, https://doi.org/10.1016/j.jobe.2021.102927.
[12] P. Artuso, G. Tosato, A. Rossetti, S. Marinetti, A. Hafner, K. Banasiak, S. Minetto, Dynamic modelling and validation of an air-to-water reversible r744 heat pump for high energy demand buildings, Energies (Basel) 14 (2021), https://doi.org/10.3390/en14248238.
[13] E. Brodal, S. Jackson, A comparative study of CO2 heat pump performance for combined space and hot water heating, Int. J. Refrig 108 (2019) 234–245, https://doi.org/10.1016/j.ijrefrig.2019.08.019.
[14] A. Zendehboudi, Energy, exergy, and exergoeconomic analyses of an air source transcritical CO2 heat pump for simultaneous domestic hot water and space heating, Energy 290 (2024) 130295, https://doi.org/10.1016/J.ENERGY.2024.130295.
[15] R.A. Otón-Martínez, F. Illán-Gómez, J.R. García-Cascales, F.J.S. Velasco, M. Reda Haddouche, Impact of an internal heat exchanger on a transcritical CO2 heat pump under optimal pressure conditions: Optimal-pressure performance of CO2 heat pump with IHX, Appl. Therm. Eng. 215 (2022) 118991, https://doi.org/10.1016/J.APPLTHERMALENG.2022.118991.
[16] Y.S.K. Reddy, A.M. Guruchethan, S. Singh, S.K.K.M.P. Maiya, A. Hafner, CO_2 heat pump integrated thermal storage for domestic hot water in hotels, J. Build. Eng. 89 (2024) 109270, https://doi.org/10.1016/J.JOBE.2024.109270.
[17] K. Nawaz, B. Shen, A. Elatar, V. Baxter, O. Abdelaziz, R290 (propane) and R600a (isobutane) as natural refrigerants for residential heat pump water heaters, Appl. Therm. Eng. 127 (2017) 870–883, https://doi.org/10.1016/j.applthermaleng.2017.08.080.
[18] M. Tammaro, C. Montagud, J.M. Corberán, A.W. Mauro, R. Mastrullo, A propane water-to-water heat pump booster for sanitary hot water production: seasonal performance analysis of a new solution optimizing COP, Int. J. Refrig. 51 (2015) 59–69, https://doi.org/10.1016/j.ijrefrig.2014.12.008.
[19] F. Ju, Q. Liu, H. Wang, J. Wu, Y. Chen, Y. Du, X. Fan, H. Zheng, Experimental study on the substitution potential of R1270 and R290 in an instant heat pump for domestic hot water and their temperature distribution characteristics, Appl. Therm. Eng. 269 (2025) 126114, https://doi.org/10.1016/J.APPLTHERMALENG.2025.126114.
[20] B. Lei, H. Shi, C. Wang, J. Wu, L. Zhang, Experimental study on the performance of R290 air-water heat pump with vapor injection for cold regions, in: Proceedings of the 26th IIR International Congress of Refrigeration: Paris, France, August 21-25, 2023, 2023.
[21] M. Pitarch, E. Navarro-Peris, J. Gonzálvez-Maciá, J.M. Corberán, Evaluation of different heat pump systems for sanitary hot water production using natural refrigerants, Appl. Energy 190 (2017) 911–919, https://doi.org/10.1016/j.apenergy.2016.12.166.
[22] R. Fingas, M. Haida, J. Smolka, G. Besagni, J. Bodys, M. Palacz, A.J. Nowak, Experimental analysis of the air-to-water ejector-based R290 heat pump system for domestic application, Appl. Therm. Eng. 236 (2024) 121800, https://doi.org/10.1016/J.APPLTHERMALENG.2023.121800.
[23] M. Tammaro, C. Montagud, J.M. Corberán, A.W. Mauro, R. Mastrullo, Seasonal performance assessment of sanitary hot water production systems using propane and CO_2 heat pumps, Int. J. Refrig 74 (2017) 224–239, https://doi.org/10.1016/j.ijrefrig.2016.09.026.
[24] W.M. Duarte, T.F. Paulino, J.J.G. Pabon, S. Sawalha, L. Machado, Refrigerants selection for a direct expansion solar assisted heat pump for domestic hot water, Sol. Energy 184 (2019) 527–538, https://doi.org/10.1016/j.solener.2019.04.027.
[25] X. Masip, E. Hervas-Blasco, E. Navarro-Peris, J.M. Corberán, Comparative analysis of the domestic hot water production with R290 and R744 heat pumps, Refrigerat. Sci. Technol. Int. Instit. Refrigerat. (2020) 543–548, https://doi.org/10.18462/iir.gl.2020.1099.
[26] S. Dubey, A.M. Guruchethan, Y. Siva Kumar Reddy, M.P. Maiya, Energy, environmental and economic analysis of low GWP refrigerant heat pumps for simultaneous heating and cooling applications, Therm. Sci. Eng. Prog. 51 (2024) 102605, https://doi.org/10.1016/j.tsep.2024.102605.
[27] O. Talaba, A. Serban, P.D. Hiris, M.C. Balan, Assessment of Replacing Gas Boilers with Heat Pumps for Hot Water Preparation in Car Washes, E3S Web of Conferences 608 (2025) 01011. https://doi.org/10.1051/e3sconf/202560801011.
[28] E. Zanetti, S. Bordignon, R. Conte, A. Bisi, M. Azzolin, A. Zarrella, Experimental and numerical analysis of a CO_2 dual-source heat pump with PVT evaporators for residential heating applications, Appl. Therm. Eng. 233 (2023) 121165, https://doi.org/10.1016/j.applthermaleng.2023.121165.
[29] R. Conte, E. Zanetti, M. Tancon, M. Azzolin, S. Girotto, D. Del Col, The advantage of running a direct expansion CO_2 heat pump with solar-and-air simultaneous heat sources: experimental and numerical investigation, Appl. Energy 369 (2024), https://doi.org/10.1016/j.apenergy.2024.123478.
[30] E. Zanetti, M. Azzolin, R. Conte, S. Girotto, D. Del Col, Experiments and dynamic modelling of dry expansion and flooded evaporators in a CO2 solar assisted heat pump, Appl. Therm. Eng. 217 (2022), https://doi.org/10.1016/j.applthermaleng.2022.118964.
[31] E. Zanetti, M. Azzolin, S. Girotto, D. Del Col, Performance and control of a CO_2 dual source solar assisted heat pump with a photovoltaic-thermal evaporator, Appl. Therm. Eng. 218 (2023), https://doi.org/10.1016/j.applthermaleng.2022.119286.
[32] M. Lee, S.H. Ham, S. Lee, J. Kim, Y. Kim, Multi-objective optimization of solar-assisted ground-source heat pumps for minimizing life-cycle cost and climate performance in heating-dominated regions, Energy 270 (2023) 126868, https://doi.org/10.1016/J.ENERGY.2023.126868.
[33] E. Zanetti, M. Azzolin, S. Bortolin, G. Busato, D. Del Col, Experimental data and modelling of a dual source reversible heat pump equipped with a minichannels evaporator, Therm. Sci. Eng. Prog. 35 (2022) 101471, https://doi.org/10.1016/J.TSEP.2022.101471.
[34] G.A. Longo, G. Righetti, C. Zilio, A new computational procedure for refrigerant condensation inside herringbone-type brazed plate heat exchangers, Int. J. Heat Mass Transf. 82 (2015) 530–536, https://doi.org/10.1016/j.ijheatmasstransfer.2014.11.032.
[35] A. Zendehboudi, Z. Ye, A. Hafner, T. Andresen, G. Skaugen, Heat transfer and pressure drop of supercritical CO_2 in brazed plate heat exchangers of the tri-partite gas cooler, Int. J. Heat Mass Transf. 178 (2021) 121641, https://doi.org/10.1016/J.IJHEATMASSTRANSFER.2021.121641.
[36] H. Martin, A theoretical approach to predict the performance of chevron-type plate heat exchangers, Chem. Eng. Process. Intensific. 35 (1996) 301–310, https://doi.org/10.1016/0255-2701(95)04129-X.
[37] E.W. Lemmon, I.H. Bell, M.L. Huber, M.O. McLinden, NIST Standard Reference Database 23: Reference Fluid Thermodynamic and Transport Properties-REFPROP, Version 10.0, National Institute of Standards and Technology, (2018). https://www.nist.gov/srd/refprop.
[38] K.G. Schmidt, M1 Heat Transfer to Finned Tubes, in: VDI Heat Atlas, Springer-Verlag, 1991. https://doi.org/10.1007/978-3-540-77877-6_94.
[39] J.L. Threlkeld, Thermal environmental engineering, 1970.
[40] M.H. Kim, C.W. Bullard, Air-side performance of brazed aluminum heat exchangers under dehumidifying conditions, Int. J. Refrig 25 (2002) 924–934, https://doi.org/10.1016/S0140-7007(01)00106-2.
[41] Z. Liu, R.H.S. Winterton, A general correlation for saturated and subcooled flow boiling in tubes and annuli, based on a nucleate pool boiling equation, Int. J. Heat Mass Transf. 34 (1991) 2759–2766, https://doi.org/10.1016/0017-9310(91)90234-6.
[42] L. Wojtan, T. Ursenbacher, J.R. Thome, Investigation of flow boiling in horizontal tubes: Part II—Development of a new heat transfer model for stratified-wavy, dryout and mist flow regimes, Int. J. Heat Mass Transf. 48 (2005) 2970–2985, https://doi.org/10.1016/J.IJHEATMASSTRANSFER.2004.12.013.
[43] V. Gnielinski, New equations for heat and mass transfer in turbulent pipe and channel flow, Int. Chem. Eng. 16 (1976) 359–368.

[44] D.G. Rich, Effect of fin spacing on the heat transfer and friction performance of multi-row, smooth plate fin-and-tube heat exchangers, in, ASHRAE Trans. (1973) 137–145.
[45] M. Abu Madi, R.A. Johns, M.R. Heikal, Performance characteristics correlation for round tube and plate finned heat exchangers: equations relatives aux performances d'échangeurs de chaleur constitués de tubes ronds et de plaques à ailettes, Int. J. Refrig. 21 (1998) 507–517, https://doi.org/10.1016/S0140-7007(98)00031-0.
[46] J. Wang, E. Hihara, Prediction of air coil performance under partially wet and totally wet cooling conditions using equivalent dry-bulb temperature method, Int. J. Refrig. 26 (2003) 293–301, https://doi.org/10.1016/S0140-7007(02)00132-9.
[47] BS EN ISO 9806, BS EN ISO 9806: 2017 Solar energy. Solar thermal collectors. Test methods, British Standards. BSI Standards Limited 2018, (2017).
[48] J.A. Duffie, W.A. Beckman, Solar Eng. Therm. Process. (1982), https://doi.org/10.1016/0142-694x(82)90016-3.
[49] EN 12900:2013, EN 12900:2013, Refrigerant compressors — Rating conditions, tolerances and presentation of manufacturer's performance data, (2013).
[50] AHRI, AHRI Standard 540: Performance rating of positive displacement refrigerant compressors, (2020).
[51] A. Rahman, A.D. Smith, N. Fumo, Performance modeling and parametric study of a stratified water thermal storage tank, Appl. Therm. Eng. 100 (2016) 668–679, https://doi.org/10.1016/j.applthermaleng.2016.01.163.
[52] I. De la Cruz-Loredo, D. Zinsmeister, T. Lickleder, C.E. Ugalde-Loo, D.A. Morales, H. Bastida, V.S. Perić, A. Saleem, Experimental validation of a hybrid 1-D multi-node model of a hot water thermal energy storage tank, Appl. Energy 332 (2023) 120556, https://doi.org/10.1016/J.APENERGY.2022.120556.
[53] X. Yang, S. Svendsen, Improving the district heating operation by innovative layout and control strategy of the hot water storage tank, Energ. Buildings 224 (2020) 110273, https://doi.org/10.1016/j.enbuild.2020.110273.
[54] K. Dqg, X.F.D. Huudulql, A predictive control strategy for energy management in building with radiant floors and thermal storage, 5 (2018).
[55] Frascold, FSS3, FRASCOLD SELECTION SOFTWARE, (n.d.). https://www.frascold.it/public/files/FSS3-Setup_-_NoAdmin.exe.
[56] M. Pitarch, E. Hervas-Blasco, E. Navarro-Peris, J. Gonzálvez-Maciá, J.M. Corberán, Evaluation of optimal subcooling in subcritical heat pump systems, Int. J. Refrig. 78 (2017) 18–31, https://doi.org/10.1016/j.ijrefrig.2017.03.015.
[57] Gestore dei Servizi Energetici S.p.A., Rapporto Statistico 2023 Solare Fotovoltaico, 2024. https://www.gse.it/documenti_site/Documenti%20GSE/Rapporti%20statistici/Solare%20Fotovoltaico%20-%20Rapporto%20Statistico%202023.pdf (accessed January 9, 2025).
[58] EnergyPlus database, (2024). https://energyplus.net/weather.
[59] D. Ivanko, H.T. Walnum, N. Nord, Development and analysis of hourly DHW heat use profiles in nursing homes in Norway, Energ. Buildings 222 (2020), https://doi.org/10.1016/j.enbuild.2020.110070.
[60] S. Murakawa, D. Nishina, H. Takata, A. Tanaka, An Analysis on the Loads of Hot Water Consumption in the Restaurants, in: CIB W062 Symposium, 2005.